Length-scale cascade and spray expansion for planar liquid jets

A. Zandian[1]†, W. A. Sirignano[1] and F. Hussain[2]

[1]Department of Mechanical and Aerospace Engineering, University of California, Irvine, CA 92697, USA

[2]Department of Mechanical Engineering, Texas Tech University, Lubbock, TX 79409, USA

(Received xx; revised xx; accepted xx)

The breakup region of a planar liquid jet is explored via direct numerical simulation (DNS) of the incompressible Navier-Stokes equation with level-set and volume-of-fluid surface tracking methods. PDFs of the local radius of curvature and the local cross-flow location of the liquid-gas interface are studied over wide ranges of Reynolds number (Re), Weber number (We), density ratio and viscosity ratio. PDFs differ in different atomization domains. With increasing We, the average radius of curvature decreases, the number of small droplets increases, and the cascade occurs at a faster rate. Both the mean and the standard deviation of the length scales decrease in time. The spray angle is larger at higher We, at higher density ratios, and at lower Re. Both the mean and the standard deviation of the spray size increase with time. Viscosity ratio has negligible effect on both the droplet-size distribution and spray angle. Increasing the sheet thickness however, decreases the spray angle and its growth rate, while decreasing the structure cascade rate and increasing droplet size. The asymptotic droplet size is affected more by surface tension and liquid inertia than by the liquid viscosity. Gas inertia and liquid surface tension, on the other hand, are the key parameters determining the spray angle.

1. Introduction

Atomization, the process by which a liquid stream disintegrates into droplets, is a fluid mechanics phenomenon having numerous industrial, automotive, environmental, as well as aerospace applications. Among the many engineering applications, atomization of liquid fuels in energy conversion devices is important because it governs the spread rate of the liquid jet (i.e. spray angle), size of fuel droplets, and droplet evaporation rate. Therefore, atomization affects the homogeneity of the spray mixture. The spray angle is also a key parameter to be controlled, that measures the liquid sheet instability amplitude.

The common purpose of breaking a liquid stream into spray is to increase the liquid surface area so that subsequent heat and mass transfer can be increased or a coating can be obtained. The spatial distribution, or dispersion, of the droplets is important in combustion systems because it affects the mixing of the fuel with the oxidant, hence the flame length and thickness. The size, velocity, volume flux, and number density of droplets in sprays critically affect the heat, mass, and momentum transport processes, which, in turn, affect the flame stability and ignition characteristics. Reduction in the drop size leads to higher volumetric heat release rates, wider burning ranges, and lower pollutant emissions. In other applications, however, small droplets must be avoided because their

† Email address for correspondence: azandian@uci.edu

settling velocity is low and, under certain meteorological conditions, they can draft too far downwind (Negeed *et al.* 2011).

Most previous researches have attempted to assess the manner by which the final droplet-size distribution is affected by gas and liquid properties, and by the geometry of the nozzle (Dombrowski & Hooper 1962; Senecal *et al.* 1999; Mansour & Chigier 1990; Stapper *et al.* 1992; Lozano *et al.* 2001; Carvalho *et al.* 2002; Varga *et al.* 2003; Marmottant & Villermaux 2004; Negeed *et al.* 2011). General conclusions are that the Sauter Mean Diameter (SMD $= \Sigma N_i d_i^3 / \Sigma N_i d_i^2$, where N_i is the number of droplets per unit volume in size class i, and d_i is the droplet diameter) decreases with increasing relative air/liquid velocity, increasing liquid density, and decreasing surface tension, while viscosity is found to have little or no effect (Stapper *et al.* 1992). While the main focus has been on the final droplet-size distribution and the spatial growth of the spray (spray angle), little emphasis has been placed on the temporal cascade of the droplet size and the expansion rate of the spray in primary atomization. This is our main focus - better understanding of the breakup cascade should allow better control and optimization. The data presented here on spray formation is useful in the analysis and design of spray injection.

A brief review of the most important literature on the effects of the key flow parameters on spray formation, droplet-size distribution, and spray angle is now provided, followed by the main objectives of this study

1.1. *Analytical studies*

Dombrowski & Hooper (1962) developed theoretical expressions for the size of drops produced from fan spray sheets. They showed that under certain operating conditions in super atmospheric pressures, the drop size increases with ambient density. Verified experimentally, the drop size initially decreases, passing through a minimum with further increase of ambient density. They also showed that, for relatively thin sheets ($h/\lambda < 1.25$; h is sheet thickness and λ is the unstable wavelength), the drop size depends directly on the surface tension and the liquid density, but inversely on the liquid injection pressure and the gas density. For relatively thick sheets ($h/\lambda > 1.5$), however, the drop size is independent of surface tension or injection pressure and increases with increasing gas density.

Senecal *et al.* (1999) in their linear stability analysis of liquid sheets, derived expressions for the ligament diameter for short and long waves. They showed that the ligament diameter is directly proportional to the sheet thickness, but inversely to the square root of the gas Weber number (We_g). They also analytically related the final droplet size to the ligament diameter and the Ohnesorge number ($Oh = \sqrt{We}/Re$), and showed that the SMD decreases with time. The gas viscosity and the nonlinear physics of the problem, however, were neglected.

1.2. *Experimental studies*

Effects of mean drop size and velocity on liquid sheets were measured using a phase Doppler particle analyzer (PDPA) by Mansour & Chigier (1990). The spray angle decreased notably with increasing liquid flow rate while maintaining the same air pressure. They related this behavior to the reduction in the specific energy of air per unit volume of liquid leaving the nozzle. Increasing the air pressure for a fixed liquid flow rate resulted in an increase in the spray angle.

Mansour & Chigier (1990) also measured the SMD along and across the spray axis. SMD initially decreased followed by a gradual increase along the spray axis - the initial

decrease due to secondary atomization and the subsequent increase due to droplet coalescence. At all axial locations, SMD increased substantially from the central part toward the edge of the spray. The larger droplets seen around the rims of the sheet were due to the mechanical effects of the lower air-liquid relative velocity on the sheet edges. They also showed a significant reduction in droplet size by increasing the air-to-liquid mass-flux ratio.

Lozano *et al.* (2001) correlated physical fluid properties, nozzle geometry and flow conditions with the mean droplet diameter, obtained by laser diffractometry. They found that the mean diameter decreases with increasing gas velocity. For a fixed gas velocity, and different liquid velocities, the mean diameter has a minimum near the frequency maximum. At large downstream distances for a fixed gas velocity, the diameter always decreases with increasing momentum flux ratio, due to secondary breakup.

Carvalho *et al.* (2002) performed detailed measurements of the spray angle versus gas and liquid velocities in a planar liquid film surrounded by two air streams in a range of the Reynolds number (Re) from 500 to 5000. For low gas-to-liquid momentum ratio, the dilatational wave dominates the liquid film disintegration mode. The atomization quality is rather poor, with a narrow spray angle. For higher gas-to-liquid momentum ratios, sinusoidal waves dominate and the atomization quality is considerably improved, as the spray angle increases significantly. Regardless of the gas velocity, a region of maximum spray angle occurs, followed by a sharp decrease for higher values of the liquid velocity, and the maximum value of the spray angle decreases with the gas flow rate.

At present, it is not possible to predict the droplet diameter distribution as a function of injection conditions. For combustion applications, many empirical correlations predict the droplet size as a function of injection parameters (Lefebvre 1989); however, more detailed studies of fundamental breakup mechanisms are needed to construct predictive models. A summary of several of these expressions for airblast atomization was compiled by Lefebvre (1989). The dependence of the primary droplet size (d) on the atomizing gas velocity (U_g) is most often expressed as a power law, $d \propto U_g^{-n}$, where $0.7 \leqslant n \leqslant 1.5$. Physical explanations for particular values of the exponent n are generally lacking. Varga *et al.* (2003) found that the mean droplet size is not very sensitive to the liquid jet diameter - actually opposite to intuition; the droplet size is observed to increase slightly with decreasing nozzle diameter. This effect was attributed to the slightly longer gas boundary-layer attachment length. They also observed a clear reduction in droplet size with lowering surface tension. The ratio of the water SMD to the ethanol SMD appeared to be very close to $\sqrt{\sigma_{water}/\sigma_{ethanol}} \approx \sqrt{3}$, which suggests the scaling $d \propto We_g^{-1/2}$, where We_g is the Weber number based on gas properties and jet diameter. Their study was limited to very low Oh ($\sim 10^{-3}$).

Marmottant & Villermaux (2004) presented probability density functions (PDF) of the ligament size and the droplet size in their experimental study of the round liquid spray formation. The ligament size d_0 was found to be distributed around the mean in a nearly Gaussian distribution, but the droplet diameter d was more broadly distributed and skewed. Rescaled by d_0, which depends on the gas velocity U_g, the size distribution keeps roughly the same shape for various gas flows. The average droplet size after ligament breakup was found to be $d \simeq 0.4 d_0$, with its distribution $P(d)$ having an exponential fall-off at large diameters parameterized by the average ligament size $\langle d_0 \rangle$, $P(d) \sim \exp(-nd/\langle d_0 \rangle)$. The parameter $n \approx 3.5$ slowly increased with U_g. The mean droplet size in the spray decreases like U_g^{-1}. Most of their experiments were at low Re and low We range.

More recently, Negeed *et al.* (2011) analytically and experimentally studied the effects

of nozzle shape and spray pressure on the liquid sheet characteristics. They showed that the droplet mass mean diameter decreases by increasing the water sheet Re or by increasing the water sheet We, since the inertia force increases by increasing both parameters. The spray pressure difference was also shown to have a similar effect to Re on the mean droplet size. Their study was limited to very high Re's (10 000–36 000) and very low We's ($\sim O(10^1)$).

1.3. *Computational studies*

In the past few years, more computational studies have addressed the liquid-jet breakup length scales and spray size. Most of these, however, have qualitatively investigated the effects of fluid properties and flow parameters on the final droplet size distribution or the spray angle. In only a few studies, quantitative results have been presented for the spatial variation of the droplet/ligament size along or across the spray axis. However, there were no detailed study of the temporal variation of the liquid-structure size distribution and the spray-size (spray-angle).

Desjardins & Pitsch (2010) defined the half-width of the planar jets as the distance from the jet centerline to the point at which the mean streamwise velocity excess is half of the centerline velocity. They showed that high We jets grow faster, which suggests that surface tension stabilizes the jets. They also demonstrated that, regardless of the We, droplets are generated through the creation and stretching of liquid ligaments. Ligaments are longer, thinner, and more numerous as We is increased. The corrugation length scales appear larger for lower Re - attributed to lesser energy contained in small eddies at lower Re cases. Consequently, earlier deformation on the smaller scales of the interface is more likely to take place on relatively larger length scales, as Re is reduced. Their work was limited to We of $O(10^2$–$10^3)$, which were low compared to our range of interest for common liquid fuels and high-pressure operations. The effects of density ratio were also not studied in their work.

Jarrahbashi *et al.* (2016) studied a wide ranges of density ratio (0.05–0.5), Re (320–8000), and We of $O(10^4$–$10^5)$ in round liquid jet breakup. They defined the radial scale of the two-phase mixture as the outermost radial location of the continuous liquid and showed that the radial spray growth increases with increasing gas-to-liquid density ratio. They showed that droplets are larger for higher gas densities and lower We's, and form at earlier times for higher density ratios. However, the effects of Re and We were not fully studied there.

In a similar study, Zandian *et al.* (2016) explored planar liquid jets to show the effects of We on the droplet size as well as the liquid sheet expansion rate. They also showed the variation in the size and number density of droplets for We in the range 3000–72 000; however, both these quantities were obtained from visual post-processing, which incur non-negligible errors. Their qualitative comparison showed that droplet and ligament sizes decrease with increasing We, while the number of droplets increases. Their results applied for a limited time after the injection, and did not show how fast the length scales cascade.

Zandian *et al.* (2016) similar to Jarrahbashi *et al.* (2016) defined the distance of the farthest point on the continuous liquid sheet surface from the jet centerline as the cross-flow size of the spray, as schematically illustrated in figure 1. Even though this definition provides a simple description of how far the spray has expanded, it lacks any statistical information about the liquid jet cross-section; i.e. it does not show the number density of the liquid droplets or ligaments at any cross-flow distance from the centerline. Thus, this definition is not optimal for the spray size and fails to show the effects of We on the

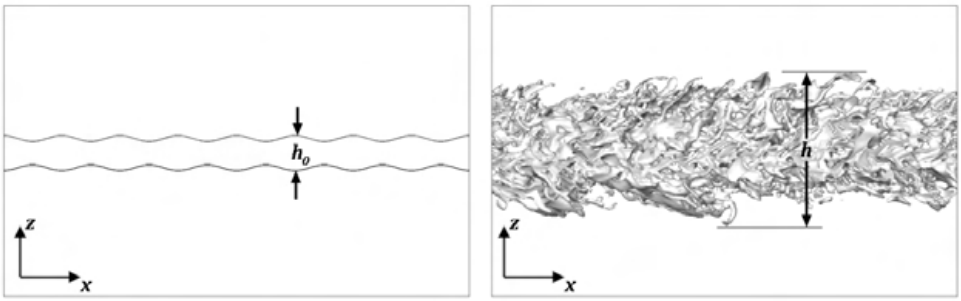

FIGURE 1. Schematic showing the spray size basis as defined by Zandian *et al.* (2016).

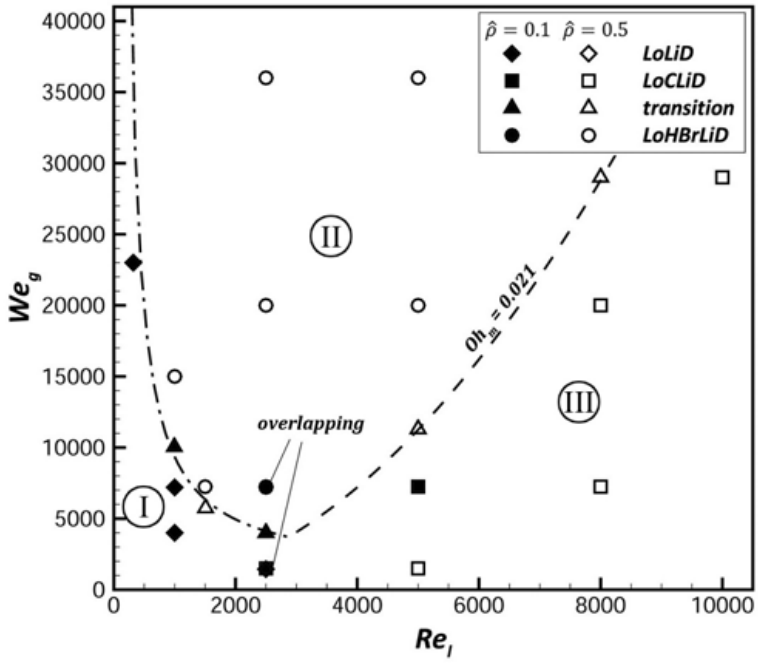

FIGURE 2. The breakup characteristics based on We_g and Re_l, showing the $LoLiD$ mechanism (Atomization Domain I) denoted by diamonds, the $LoHBrLiD$ mechanism (Atomization Domain II) denoted by circles, the $LoCLiD$ mechanism (Atomization Domain III) denoted by squares, and the transitional region denoted by triangles. The cases with density ratio of 0.1 ($\hat{\rho} = 0.1$) are shaded. The $\hat{\rho} = 0.1$ and $\hat{\rho} = 0.5$ cases that overlap at the same point on this diagram are noted. $-\cdot-\cdot-$, transitional boundary at low Re_l; and $- - -$, transitional boundary at high Re_l (Zandian *et al.* 2017*b*).

spray expansion rate. The effects of Re and density ratio were not studied in detail in their work.

In the most recent work, Zandian *et al.* (2017*b*) identified three atomization mechanisms and defined their domains of dominance on a gas Weber number (We_g) versus liquid Reynolds number (Re_l) diagram, as shown in figure 2. The liquid structures seen in each of these atomization domains are sketched in figure 3, where the evolution of a liquid lobe is shown from a top view. At high Re_l, the liquid sheet breakup characteristics change based on a modified Ohnesorge number, $Oh_m \equiv \sqrt{We_g}/Re_l$, as follows: (i) at high Oh_m and high We_g, lobes become thin and puncture, creating holes and bridges. Bridges break as perforations expand and create ligaments, which then stretch and break into droplets by capillary action. This domain is indicated as Atomization Domain II in figure 2, and its process was called $LoHBrLiD$ based on the cascade of structures in this domain ($Lo \equiv$ Lobe, $H \equiv$ Hole, $Br \equiv$ Bridge, $Li \equiv$ Ligament, and $D \equiv$ Droplet); (ii) at low Oh_m and high Re_l, holes are not seen at early times; instead, many corrugations form on the lobe

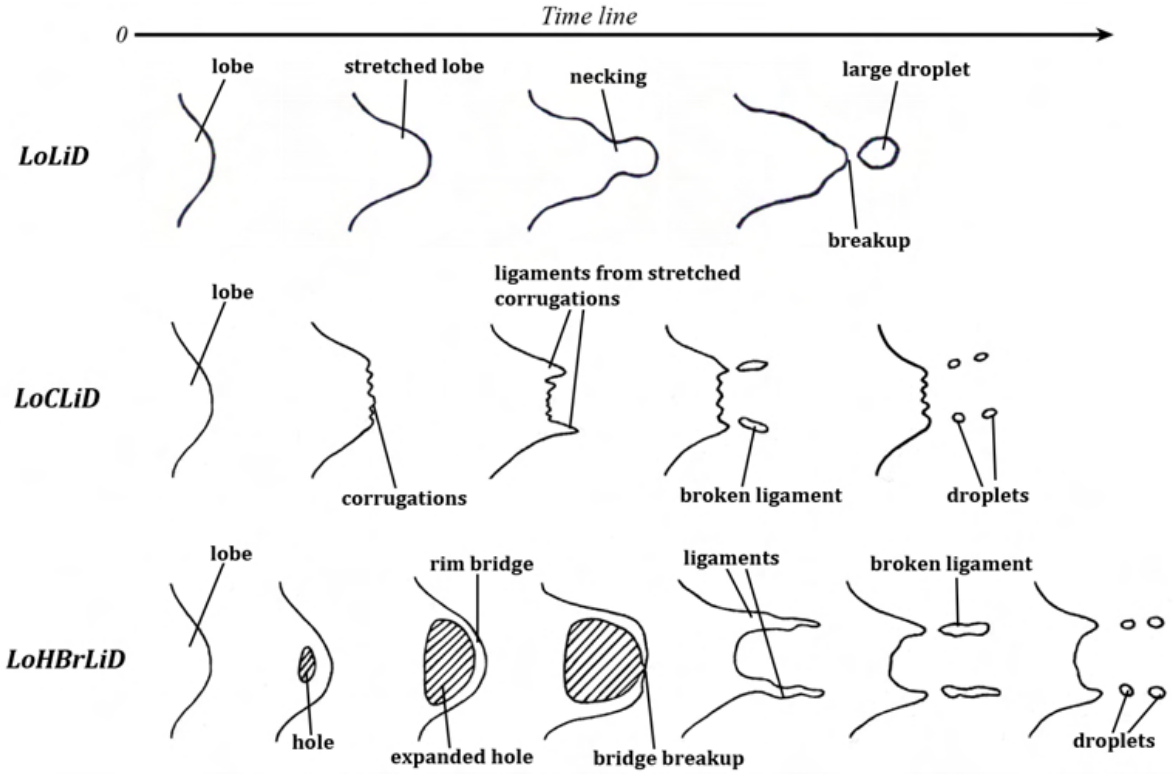

FIGURE 3. Sketch showing the cascade of structures on a liquid lobe from a top view, for the $LoLiD$ (top), $LoCLiD$ (center), and $LoHBrLiD$ (bottom) processes. The gas flows on top of these structures from left to right, and time increases to the right (Zandian *et al.* 2017*b*).

front edge and stretch into ligaments. This process is called $LoCLiD$ ($C \equiv$ Corrugation) and occurs in Atomization Domain III (see figure 2), and results in ligaments and droplets without having the hole and bridge formation steps. The third process follows a $LoLiD$ process and occurs at low Re_l and low We_g (Atomization Domain I in figure 2), but with some difference in details from the $LoCLiD$ process.

The main difference between the two processes at high and low Re_l's is that, at higher Re_l the lobes become corrugated before stretching into ligaments. Hence, each lobe may produce multiple ligaments, which are typically thinner and shorter than those at lower Re_l. At low Re_l, on the other hand, because of the higher viscosity, the entire lobe stretches into one thick, usually long ligament. There is also a transitional region between the atomization domains, shown by the dashed-lines in figure 2. As seen in figure 3, the primary atomization follows a cascade process, where larger liquid structures, e.g. waves and lobes, cascade into smaller and smaller structures; e.g. bridges, corrugations, ligaments, and droplets. The time scale of the structure formations was also determined and correlations were found by Zandian *et al.* (2017*b*). However, the length scale of the structures observed in each domain and their cascade rate was not discussed. This will be accomplished here.

1.4. *Objectives*

Our objectives are to (i) study the effects of the key non-dimensional parameters, i.e. Re, We, gas-to-liquid density ratio and viscosity ratio, and the wavelength-to-sheet-thickness ratio, on the temporal variation of the spray size and the liquid-structures length scale; (ii) establish a new model and definition for measurement of the droplet-size distribution and spray size; and (iii) explain the roles different breakup regimes play in the final droplet-size distribution and spray growth. The results are separated by

atomization domains to clarify the effects of each atomization mechanism on the cascade process and spray expansion. Moreover, the time portions of the behavior are related to the various structure formations.

To address the objectives, two probability density functions (PDF) are obtained from the numerical results, for a wide range of liquid-structure size and transverse location of the liquid-gas interface at different times, to give a broader understanding of the temporal variation of the length-scale distribution and the spray size. The time-dependent behavior of the distribution functions is given rather than just the long-time asymptotic length scales, as is well explored and examined in the literature. The first PDF indicates the size of the small liquid structures; i.e. lobes, bridges, ligaments, and droplets. The second PDF indicates the location of the liquid-gas interface, giving more than just the outermost location of the spray, as is accounted for in most past computational studies. Thus, a more meaningful and realistic presentation of the spray size is provided by these PDFs.

In §2, the numerical methods that have been used and the most important flow parameters involved in this study are presented, along with the post-processing methods that have been used to obtain the PDFs. Section 3 is devoted to the analysis of the effects of We (§3.2), Re (§3.3), density ratio (§3.4), viscosity ratio (§3.5), and sheet thickness (§3.6) on the spray growth and the liquid-structure size. Conclusions are given in §4, accompanied by a short summary of our most important findings.

2. Numerical Modeling

The three-dimensional Navier-Stokes equations with level-set and volume-of-fluid surface tracking methods yield computational results for the liquid segment which captures the liquid-gas interface deformations with time.

The incompressible continuity and Navier-Stokes equations, including the viscous diffusion and surface tension forces and neglecting the gravitational force, are as follows;

$$\boldsymbol{\nabla} \cdot \boldsymbol{u} = 0, \tag{2.1}$$

$$\frac{\partial(\rho \boldsymbol{u})}{\partial t} + \boldsymbol{\nabla} \cdot (\rho \boldsymbol{u}\boldsymbol{u}) = -\boldsymbol{\nabla} p + \boldsymbol{\nabla} \cdot (2\mu \boldsymbol{D}) - \sigma\kappa\delta(d)\boldsymbol{n}, \tag{2.2}$$

where $\boldsymbol{D}$ is the rate of deformation tensor,

$$\boldsymbol{D} = \frac{1}{2}\left[(\boldsymbol{\nabla u}) + (\boldsymbol{\nabla u})^T\right]. \tag{2.3}$$

$\boldsymbol{u}$ is the velocity field; p, ρ, and μ are the pressure, density and dynamic viscosity of the fluid, respectively. The last term in equation (2.2) is the surface tension force per unit volume, where σ is the surface tension coefficient, κ is the surface curvature, $\delta(d)$ is the Dirac delta function, d is the distance from the interface, and $\boldsymbol{n}$ is the unit vector normal to the liquid/gas interface.

Direct numerical simulation is done with an unsteady three-dimensional finite-volume solver for the incompressible Navier-Stokes equations describing the planar liquid sheet segment (initially stagnant), which is subject to instabilities due to a gas stream that flows past it on both sides. A uniform staggered grid is used with the mesh size of 2.5 μm and a time step of 5 ns - finer grid resolution of 1.5 μm is used for the case with higher We_g (= 115 000). Spatial discretization and time marching are given by the third-order accurate QUICK scheme and the Crank-Nicolson scheme, respectively. The continuity and momentum equations are coupled through the SIMPLE algorithm.

The level-set method developed by Osher and his coworkers (Zhao *et al.* 1996; Sussman *et al.* 1998; Osher & Fedkiw 2001) captures the liquid-gas interface. The level set ϕ is a

distance function with zero value at the liquid-gas interface, positive values in the gas phase and negative values in the liquid phase. All the fluid properties for both phases in the Navier-Stokes equations are defined based on the ϕ value and the equations are solved for both phases simultaneously. Properties such as density and viscosity vary continuously but with a very large gradient near the liquid-gas interface. The level-set function ϕ is also advected by the velocity field;

$$\frac{\partial \phi}{\partial t} + \boldsymbol{u} \cdot \boldsymbol{\nabla} \phi = 0. \tag{2.4}$$

For detailed descriptions for this interface tracking see Sussman *et al.* (1998).

At low density ratios, a transport equation similar to equation (2.4) is used for the volume fraction f, also called the Volume-of-Fluid (VoF) variable, in order to describe the temporal and spatial evolution of the two phase flow (Hirt & Nichols 1981). The VoF-variable f, introduced by Hirt & Nichols (1981), represents the volume of (liquid phase) fluid fraction in each cell.

The fully conservative momentum convection and volume fraction transport, the momentum diffusion, and the surface tension are treated explicitly. To ensure a sharp interface of all flow discontinuities and to suppress numerical dissipation of the liquid phase, the interface is reconstructed at each time step by the PLIC (piecewise linear interface calculation) method of Rider & Kothe (1998). The liquid phase is transported on the basis of its reconstructed distribution. The capillary effects in the momentum equations are represented by a capillary tensor (Scardovelli & Zaleski 1999).

2.1. *Flow Configuration*

The computational domain, shown in figure 4, consists of a cube, which is discretized into uniform-sized cells. The liquid segment, which is a sheet of thickness h_0 ($h_0 = 50$ μm for the thin sheet and 200 μm for the thick sheet in this study), is located at the center of the box and is stationary in the beginning. The domain size in terms of the sheet thickness is $16h_0 \times 10h_0 \times 10h_0$, in the x, y and z directions, respectively, for the thin sheet, and $4h_0 \times 4h_0 \times 8h_0$ for the thick sheet. The liquid segment is surrounded by the gas zones on top and bottom. The gas moves in the positive x- (streamwise) direction with a constant velocity ($U = 100$ m/s) at the top and bottom boundaries, and its velocity diminishes to the interface velocity with a boundary layer thickness obtained from 2D full jet simulations. In the liquid, the velocity decays to zero at the center of the sheet with a hyperbolic tangent profile. For more detailed description of the initial conditions, see figure 12 of Zandian *et al.* (2016).

The liquid-gas interface is initially perturbed symmetrically on both sides with a sinusoidal profile and predefined wavelength and amplitude. Both streamwise (x-direction) and spanwise (y-direction) perturbations are considered in this study. Periodic boundary conditions for all components of velocity as well as the level-set/VoF variable are imposed on the four sides of the computational domain; i.e. the x- and y-planes.

The most important dimensionless groups in this study are the Reynolds number (Re), the Weber number (We), as well as the gas-to-liquid density ratio ($\hat{\rho}$) and viscosity ratio ($\hat{\mu}$), as defined below. The initial wavelength-to-sheet-thickness ratio (Λ) is also an important parameter.

$$Re = \frac{\rho_l U h_0}{\mu_l}, \quad We = \frac{\rho_l U^2 h_0}{\sigma}, \quad \hat{\rho} = \frac{\rho_g}{\rho_l}, \quad \hat{\mu} = \frac{\mu_g}{\mu_l}, \quad \Lambda = \frac{\lambda_0}{h_0}. \tag{2.5}$$

The sheet thickness h_0 and the velocity of the far field gas U are considered as the

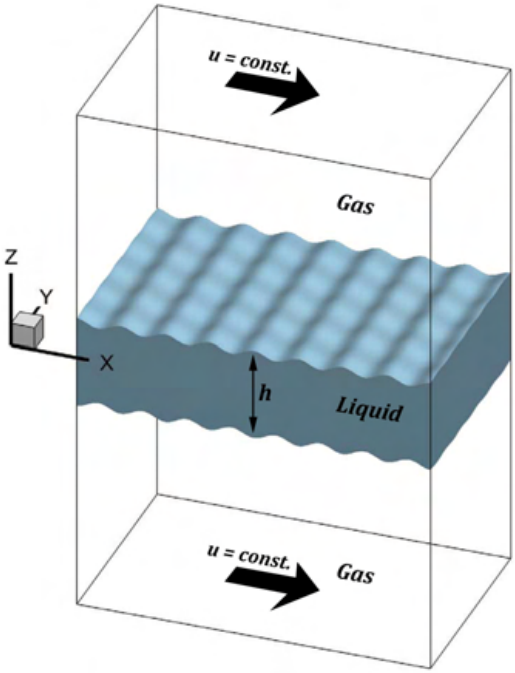

FIGURE 4. The computational domain with the initial liquid and gas zones.

characteristic length and velocity, respectively. The subscripts l and g refer to the liquid and gas, respectively.

The grid independency tests were performed previously by Jarrahbashi & Sirignano (2014), Jarrahbashi *et al.* (2016), and Zandian *et al.* (2016). They showed that the errors in the size of the ligaments, penetration length of the liquid jet and the magnitude of the velocity computed using different mesh resolutions were within an acceptable range. The effects of the mesh size, the thickness of the fuzzy zone between the two phases - where properties have large gradients to approximate the discontinuities - and mass conservation of the level-set method have been previously addressed by Jarrahbashi & Sirignano (2014). The domain-size independency was also checked in both streamwise and spanwise directions to ensure that the resolved wavelengths were not affected by the domain length and width. The normal dimension of the domain was chosen such that the top and bottom boundaries remain far from the interface at all times, so that the surface deformation is not directly affected by the boundary conditions. In addition, accuracy tests and validation with experiments and other numerical approaches were performed previously (Jarrahbashi & Sirignano 2014), and will not be repeated here.

2.2. *Data analysis*

Twice the inverse of the liquid surface curvature ($\kappa = \frac{1}{R_1} + \frac{1}{R_2}$, where R_1 and R_2 are the two radii of curvature of the surface in a 3D domain) has been defined as the local length scale in this study. This length scale represents the radius of curvature of the interface, which would eventually asymptote to the droplet radius. Based on this definition, a length scale is obtained at each computational cell in the fuzzy zone at the interface. The curvature of each cell containing the interface is computed at every time step since it is required for the computation of the surface tension force; then, the structure length scale is defined as

$$L_{ijk} = \frac{2}{|\kappa_{ijk}|}, \tag{2.6}$$

where κ is the curvature, and the ijk indices denote the coordinates of the cell in a three-dimensional mesh. The length scale L_{ijk} of each cell is used to create a PDF of the length scales. The κ_{ijk} value is counted per computational cell to obtain the PDFs. Only cells containing the interface are included in this analysis. We assume that a PDF normalized on a surface area basis would not differ significantly (this will be confirmed in the following section). The bin size used for the length-scale analysis is $\mathrm{d}L = \mathrm{d}x = 2.5$ μm. The probability of the length scale in the interval $(L, L + \mathrm{d}L)$ is obtained by multiplying the PDF value at that length scale $f(L)$ by the bin size:

$$prob(L \leqslant L' \leqslant L + \mathrm{d}L) \equiv P(L) = f(L)\mathrm{d}L. \tag{2.7}$$

This is an operational definition of the PDF $f(L)$. Since the probability is unitless, $f(L)$ has units of the inverse of the length scale; i.e. m^{-1}. However, in our study, the length scale is nondimensionalized by the initial wavelength. Thus, $f(L/\lambda_0)$ becomes unitless. The relation between the length-scale PDF and its probability could be derived from equation (2.7);

$$f(L/\lambda_0) = \frac{P(L/\lambda_0)}{\mathrm{d}L/\lambda_0} = 40P(L/\lambda_0), \tag{2.8}$$

where $\mathrm{d}L$ is the bin size and $\lambda_0 = 100$ μm is the initial Kelvin-Helmholtz (KH) wavelength. The probability of having the length scale in the finite interval $[a, b]$ can be determined by integrating the PDF;

$$prob(a \leqslant \frac{L}{\lambda_0} \leqslant b) \equiv P(a \leqslant \frac{L}{\lambda_0} \leqslant b) = \int_a^b f(\frac{L'}{\lambda_0})\frac{\mathrm{d}L'}{\lambda_0}. \tag{2.9}$$

In order to obtain the average length scale at each time step, the length scales should be integrated along the liquid-gas interface, and divided by the total interface area. The average length scale δ is nondimensionalized using the initial perturbation wavelength (λ_0). The average length scale is defined as

$$\delta = \frac{1}{\lambda_0}\frac{\int L\mathrm{d}s}{S} \approx \frac{1}{\lambda_0}\frac{\int L\mathrm{d}n}{N} = \frac{1}{\lambda_0}\frac{\sum L_i}{N}, \tag{2.10}$$

where S is the total surface area of the interface, and N is the total number of cells in the fuzzy zone along the interface. As described in this equation, instead of accounting for surface area in each computational cell and integrating the surface area of the interface, the number of cells that the interface crosses are counted as an approximation. Using the number of cells along the interface for computing the average length scale is satisfactory for our purpose, as will be shown in the following section.

Since the length scale L has a wide range from a few microns to infinity (if the curvature is zero at a cell), we neglect the length scales that are very large, i.e. $L > 4\lambda_0$, so that the average length scale would not be biased towards large scales due to those off values.

Similar to the length scale, a PDF is obtained for the normal (cross-flow) distance of the cells at the interface (at the fuzzy zone) from the centerplane. This PDF also has units of m^{-1}, as discussed before; however, it is normalized by the initial sheet thickness, so it becomes dimensionless. This gives a better statistical data about the distribution of the normal coordinate of the spray interface (spray size). To account for both sides of the liquid sheet in this analysis, the cross-flow distance h of each local point at the interface is defined as the absolute value of its z-coordinate ($z = 0$ at the centerplane);

$$h_{ijk} = |z_{ijk}|. \tag{2.11}$$

The probability of the spray size is obtained from an equation similar to equation

(2.7), where L is replaced by h. The relation between the spray-size PDF $f(h/h_0)$ and its probability $P(h/h_0)$ is

$$f(h/h_0) = \frac{P(h/h_0)}{\mathrm{d}h/h_0} = 20P(h/h_0), \tag{2.12}$$

where $\mathrm{d}h$ is the bin size for the spray-size PDF, taken to be equal to the mesh size, i.e. $\mathrm{d}h = \mathrm{d}x = 2.5$ μm, and h_0 is the initial sheet thickness; $h_0 = 50$ μm for the thin sheet, and 200 μm for the thick sheet.

The average spray size (sheet thickness) ζ is also obtained by integrating h along the interface, and dividing it by the total interface area. The mean spray size is nondimensionalized by the initial sheet thickness h_0;

$$\zeta = \frac{1}{h_0}\frac{\int h\mathrm{d}s}{S} \approx \frac{1}{h_0}\frac{\sum h_i}{N}, \tag{2.13}$$

where the cross-flow distance of the interface has been counted per computational cell. Thus, the total number of cells along the interface is counted instead of the total surface area, for simplicity. This definition represents how dense the surface is at any distance from the jet centerplane. Therefore, it gives a more realistic representation of the sheet expansion rate.

3. Results and discussion

3.1. *Data analysis verification*

The choice of bin size and the sensitivity of the post-processing method against the number of cells that are involved in the length scale computation are tested and verified in this section. The results of these tests are given in figure 5.

Figure 5(a) compares the temporal variation of the average length scale δ with two different bin sizes used for calculation of this parameter. The solid line is the result obtained by the actual bin size used in our analysis ($\mathrm{d}L = \mathrm{d}x = 2.5$ μm), and the dashed line denotes the variation of δ with time using a bin size twice as big; i.e. $\mathrm{d}L = 2\mathrm{d}x = 5$ μm. Both cases converge around 40 μs and are in good agreement thereafter. Both test cases result in the same asymptotic length scale at the end of the computation; however, in the early stages, the larger bin size produces slightly larger scales, especially around the maximum point ($t \approx 10$ μs). The maximum error in the larger bin size is around %10. The error gradually decreases after 10 μs and becomes less than %1 at 40 μs. The temporal evolution of the length scales, i.e. when the scales are growing or declining, predicted by both test cases match very well. The only difference is that the larger bin predicts larger values at the early stages. Since the magnitude in the early stage of the length scale growth (around the time when the maximum errors occur) is not the main goal of our research, it can be concluded that choosing $\mathrm{d}L = 2.5$ μm as the bin size is acceptable for the purposes of this study.

In §2.2, it was described that instead of averaging the length scale over the entire interface area, it is averaged over the number of cells containing the interface. Clearly, this simplification would result in results that are not exactly the area weighted average of the length scales. However, in figure 5(b) it is implied that this simplification results in good agreement with the real average after the liquid-jet breakup has resulted in large enough surface area. For this purpose, two cases are compared in figure 5(b) - one being the original data that is used in our study, involving all the cells that contain the interface (shown by the solid line), and the other one involving every other cell that contains the interface (shown by the dashed line). The goal here is to show that by choosing random

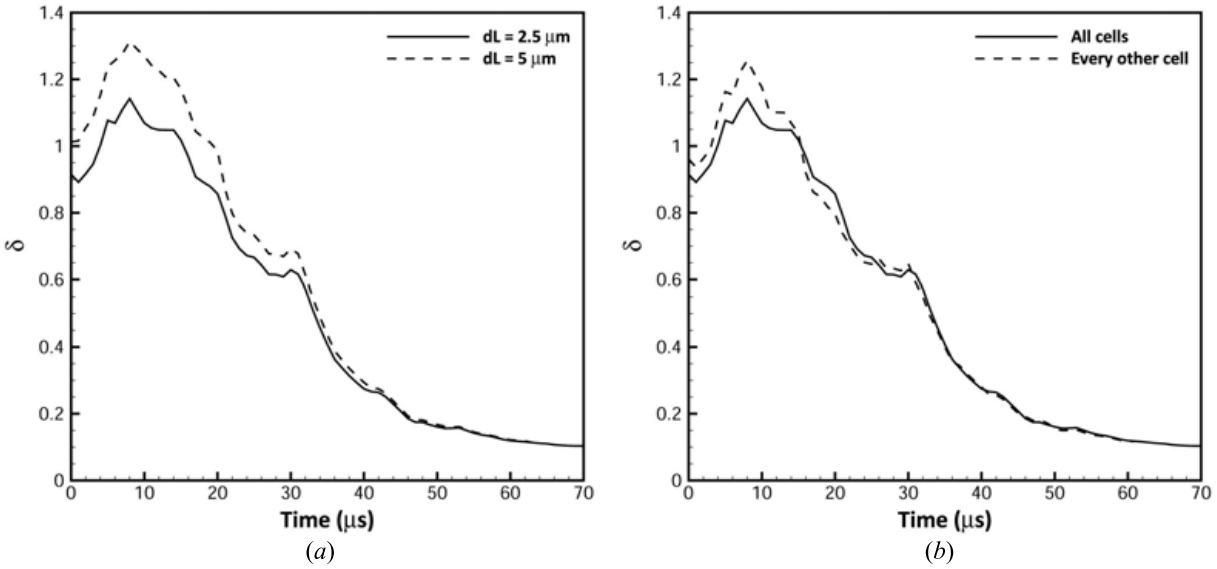

FIGURE 5. Effect of bin size on the temporal evolution of the average length scale (a); Effect of random cell selection on calculation of the temporal evolution of the average length scale (b); $Re_l = 2500$, $We_g = 7250$, $\hat{\rho} = 0.5$, $\hat{\mu} = 0.0066$, and $\Lambda = 2.0$.

cells from our data pool, very similar results are obtained compared to the case where all of the cells are considered. Since every other cell changes from one time step to another, this cell selection can be considered as being random. In other words, we are not always following the same location on the liquid surface at every time step as the surface gets stretched and deformed all the time. Therefore, we are looking at randomly selected points on the interface at each time step. Figure 5(b) shows that the results are in very good agreement after 30 μs, with less than %0.5 error. During the initial stage of the liquid sheet deformation and breakup, however, the error is larger since our data pool contains much fewer cells involved in this analysis. The maximum error is around %8, occurring around the maximum point on the curve. Since the selected cells change from one time step to another, the resulting average in the test case (dashed line) is sometimes larger than the original value (solid line), and less at other times. The result of the test case oscillates around the original case and the amplitude of this oscillation decreases as time passes; i.e. as the number of cells involved in the data analysis increases when the breakup occurs. Thus, it can be concluded that the surface area loses its significance as the number of cells involved in the analysis gets large enough. This, verifies our simplification assumption.

3.2. *Weber number effects*

The temporal variation of the average length scale for low, medium and high We_g and moderate Re_l are illustrated in figure 6. The density ratio is kept the same (0.5) among all these cases; hence, We_g is only changed through the surface tension. The effects of density ratio are analyzed in §3.4, and the combined effects of density ratio and We are revealed there. The symbols on the plot denote the first instant at which different liquid structures form during the atomization process. The definition of each symbol is introduced beside the plot in figure 6 and will be used hereafter in the proceeding plots. The symbols help us compare the rate of formation of each structure, say ligament or droplet, at different flow conditions. The relation between the formation of each structure and the behavior of the length scale or spray size can also be better understood using these symbols. The atomization domain for each process is also denoted on the plot. Note

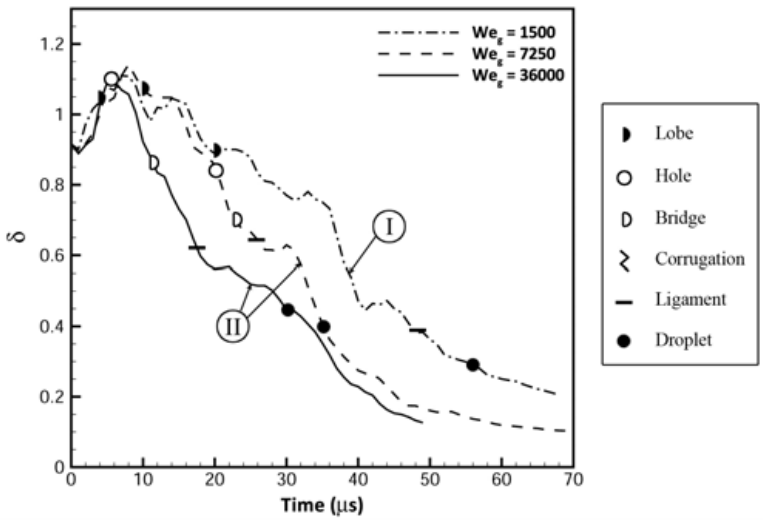

FIGURE 6. Effect of We_g on the temporal variation of the average dimensionless length scale; $Re_l = 2500$, $\hat{\rho} = 0.5$, $\hat{\mu} = 0.0066$, and $\Lambda = 2.0$. The symbols indicate the first time when different liquid structures form. The definition of each symbol is introduced beside the plot.

that the zigzag symbol denoting the "corrugation" formation does not appear in figure 6 because this structure appears only in Domain III.

The lowest We_g falls in the ligament stretching ($LoLiD$) category in Atomization Domain I, while the two higher We_g's follow the hole-formation mechanism ($LoHBrLiD$) in Domain II; see figure 2. The average length scale decreases with time for all cases, to be expected for cascade of structures presented in the earlier studies (Zandian *et al.* 2016; Jarrahbashi *et al.* 2016) (lobes to holes and bridges, to ligaments and then to droplets). The average length scale becomes smaller as We_g increases and its cascade is hastened by increasing We_g. At 40 μs, the average length scale for $We_g = 36\ 000$ is almost $0.22\lambda_0 = 22$ μm, while this increases to $0.3\lambda_0$ for $We_g = 7250$, and to $0.5\lambda_0$ at the lowest We_g. This shows the clear influence of the surface tension on the length-scale cascade and the size of the droplets. An increase in surface tension suppresses the instabilities and increases the structure size. The droplets and ligaments formed in Domain II are generally smaller than in Domain I.

The length scale starts from $0.9\lambda_0$ in all three cases due to the initial perturbations, and the average scale increases for the first 10 μs, until it reaches a maximum. We_g, and hence surface tension, does not notably affect the initial length scale growth. This growth involves the initial stretching of the waves, which creates flat regions near the braids - they have low curvatures, hence large length scales. As lobes and ligaments form later, the length scale decreases because (i) the radius of curvature of these structures is much smaller than the initial waves, and (ii) the total interface area increases by the formation of lobes, bridges, ligaments, and droplets, smearing out the influence of the large length scales. Figure 6 also shows that all the structures - especially droplets - form sooner with increasing We_g. Moreover, ligaments and droplets form slower in Domain I than in Domain II; that is, the $LoHBrLiD$ mechanism is more efficient than the $LoLiD$ process in terms of cascade rate at the same Re_l range.

Zandian *et al.* (2017*b*) showed that there are two different characteristic times for the formation of holes and the stretching of lobes and ligaments. At a given Re_l, as surface tension increases (i.e. decreasing We_g), the characteristic time for hole formation increases, thereby delaying the hole formation. Thus, for lower We_g most of the earlier ligaments are formed by direct stretching of the lobes and/or corrugations, while the hole formation is inhibited. On the other hand, at relatively large Re_l (> 3000), as liquid

viscosity is increased (i.e. decreasing Re_l), at the same We_g, the ligament-stretching time gets larger. In this case, hole formation prevails over the ligament stretching mechanism, resulting in more holes. As We_g increases, the time at which the first holes form decreases. This indicates that the hole formation time should be inversely proportional to We_g (Zandian *et al.* 2017*b*).

At low Re_l (< 3000), the liquid viscosity has an opposite effect on the hole formation and ligament stretching (Zandian *et al.* 2017*b*). As shown in figure 2, near the left boundary, the time scale of the stretching becomes relatively smaller than the hole-formation time scale as Re_l is reduced at a constant We_g. Therefore, there is a reversal to ligament stretching as Re_l is decreased at a fixed We_g. Keeping all these effects in mind, the following two nondimensional characteristic times are proposed by Zandian *et al.* (2017*b*);

$$\frac{U\tau_h}{h_0} \propto \frac{1}{We_g}\left(1+\frac{k}{Re_l}\right), \qquad \frac{U\tau_s}{h_0} \propto \frac{1}{Re_l}, \tag{3.1}$$

where τ_h and τ_s are the dimensional characteristic times for hole formation and ligament stretching, respectively, and k is a dimensionless constant. The results in figure 6 are consistent with equation 3.1, which suggests the hole formation time scale to be inversely proportional to We_g. Therefore, the hole formation time for $We_g = 36\ 000$ should be nearly 5 times smaller than for $We_g = 7250$ since Re_l is the same for both cases. From figure 6, the first instant when a hole is formed is 22 μs for $We_g = 36\ 000$ (solid line), and almost 5 μs for $We_g = 7250$ (dashed line). Thus, the ratio of τ_h for these two cases is about 4.4, in good agreement with the result obtained from equation 3.1.

Even though the average length scale gives a good insight into the temporal variation of the overall scale of the liquid structures, it does not show the distribution of the scales, for which the length-scale PDFs are needed. Figure 7 compares the probability distribution of the length scales of the three We_g's at different times on a log-scale.

All of the cases start from a somewhat bell-shaped distribution indicated by the red line. Initially, the length scales in range $0.5\lambda_0$–$0.6\lambda_0$ have the maximum probability of approximately 10%. Later, the most probable length scale becomes smaller, while the probability of the dominant size increases. The transition towards smaller scales is faster as We_g increases since lowering surface tension reduces the resistance of the liquid surface against deformations. At 50 μs, the most probable length scale becomes $0.1\lambda_0$ for $We_g = 1500$ (dashed-line in figure 7*a*). Higher We_g cases reach the same most probable length scale at 40 μs (dash-dotted line in figure 7*b*) for $We_g = 7250$, and at less than 10 μs (not shown here) for $We_g = 36\ 000$.

The PDFs also show an increase in the probability of small scales at higher We_g. At $t = 50$ μs, for example, the $We_g = 1500$ case has a probability of about 8% for the smallest computed length scale, i.e. 2.5 μm; see where the 50 μs curve intersects the vertical axis in figure 7(*a*). That probability at the same time increases to 38% as We_g increases to 7250. At even higher $We_g = 36\ 000$, the probability of 2.5 μm or lower is slightly more than 45% at 50 μs. Since the smaller length scale also implies smaller volume, the number density of the small droplets increases with We_g.

The standard deviation of the PDFs of figure 7, illustrated in figure 8, provides a more accurate quantitative measure of the length-scale distribution. The length scales range from a few microns, i.e. a small fraction of the initial wavelength, to several hundred microns, e.g. four times the initial wavelength. Therefore, the standard deviation of the normalized length scale is very large, even in the beginning. The average length scale is about $0.9\lambda_0 = 90$ μm at the start of the computations (see figure 6), but the standard deviation of the length scales is about $0.85\lambda_0 = 85$ μm.

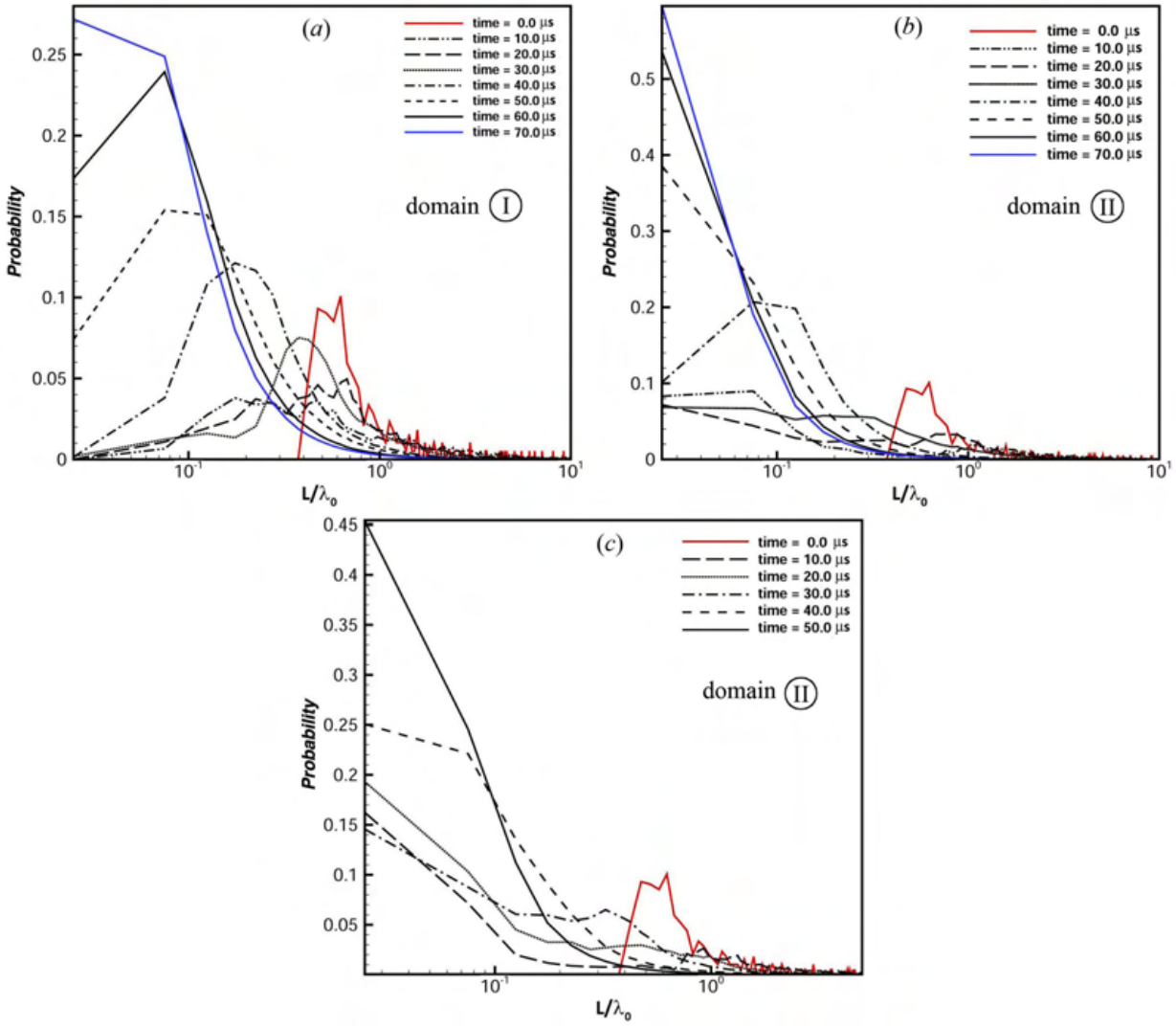

FIGURE 7. Probability distribution of the normalized length scales at different times for $We_g = 1500$ (a), $We_g = 7250$ (b), and $We_g = 36\,000$ (c); $Re_l = 2500$, $\hat{\rho} = 0.5$, $\hat{\mu} = 0.0066$, and $\Lambda = 2.0$.

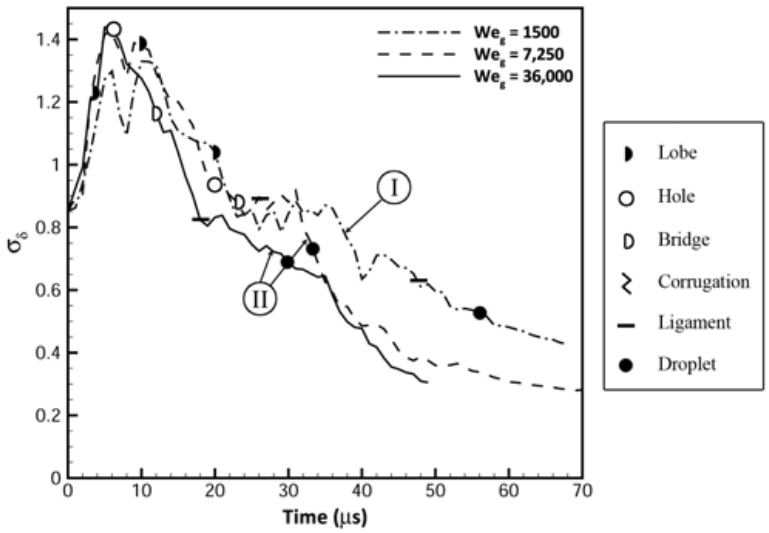

FIGURE 8. Temporal variation of the standard deviation of the dimensionless length-scale PDFs of figure 7 for $We_g = 1500$, 7250, and 36 000; $Re_l = 2500$, $\hat{\rho} = 0.5$, $\hat{\mu} = 0.0066$, and $\Lambda = 2.0$.

At the early stage, the standard deviation increases as larger scales become more probable following the flattening and stretching of the waves. Later, the flow gets filled with more small ligaments and droplets and more curved surfaces, which brings down both the mean and the standard deviation. However, even at the end of the process, the standard deviation is still around $0.4\lambda_0 = 40$ μm; so, a wide range of length scales is still present in the flow. The standard deviation decreases with increasing We_g, as the smaller capillary force allows the larger scales to deform easily and cascade more quickly into smaller scales with higher curvatures; this reduces the deviation of the scales from the mean scale.

The length scale PDFs show that: (i) the asymptotic length scale (droplet size) decreases with increasing We_g; (ii) the number of small droplets increases with increasing We_g; and (iii) the cascade of length scales occurs faster at higher We_g. The last item is also implied by the temporal evolution of the mean length scale.

As mentioned earlier, defining the jet thickness as the distance to the farthest liquid point from the centerplane does not always provide complete information and might render results which are prone to misinterpretation. This definition does not take into account the interface location distribution and only considers the farthest liquid location. For this purpose, the PDFs of the transverse interface location are used to obtain statistical results, which describe the expansion of the liquid sheet in a more meaningful form.

The effect of We_g on the temporal evolution of the average spray size is shown in figure 9 along with the liquid-jet interface picture at the end of each process. The expansion rate of the liquid jet can be distinguished better with the new definition of the sheet expansion (compare this plot with figure 40 from Zandian *et al.* 2016). The sprays expand faster at higher We_g. The average spray size remains close to the initial sheet thickness for the first 50 microseconds for $We_g = 1500$ since the high surface tension suppresses instability waves, lobe stretching, and ligament breakup. The jet expands much sooner at higher We_g; for example, at about 20 μs for $We_g = 7250$, and at 7 μs for $We_g = 36\,000$. The liquid structures stretch much quicker at higher We_g and are less suppressed by the surface tension forces; thus, they can expand more freely and are entrained more easily by the gas flow, after breakup. The expansion of the jet at the lowest We_g (dash-dotted line in figure 9) coincides with the formation of the first ligament (at 50 μs). Therefore, the lobes are much less amplified at such a low We_g and the ligament formation and stretching are primarily in the normal direction in Domain I. Generally, the spray angle is larger in Domain II than in Domain I at comparable Re_l range.

The spikes and oscillations in the average spray size ζ are caused by the detachment of a liquid structure, e.g. bridges, ligaments or droplets, from the jet core. The first reduction in the spray size coincides with the formation of the first droplets; i.e. the black circles in figure 9. The spray-size PDFs, given in figure 10, support this view.

All three cases in figure 10 start from a bell-shaped distribution around $h = h_0$, denoted by the red solid lines. The two peaks on the two sides of $h/h_0 = 1$ are due to the initial perturbations amplitude of 5 μm imposed on the surface of the sheet. Since there are more computational cells near the peak and trough of the perturbations compared to the neutral plane, i.e. $h/h_0 = 1$, the probability of those sizes are slightly higher. The probability of the initial thickness value increases in all cases during the first 20 μs since the wave amplitude decreases as the waves get distorted in the initial stage.

Later, when the waves start to grow due to the KH instability and roll-up of the lobes over the primary KH vortices, the jet thickness increases and the distribution becomes wider and skews towards larger values on the right. Meanwhile, smaller lengths

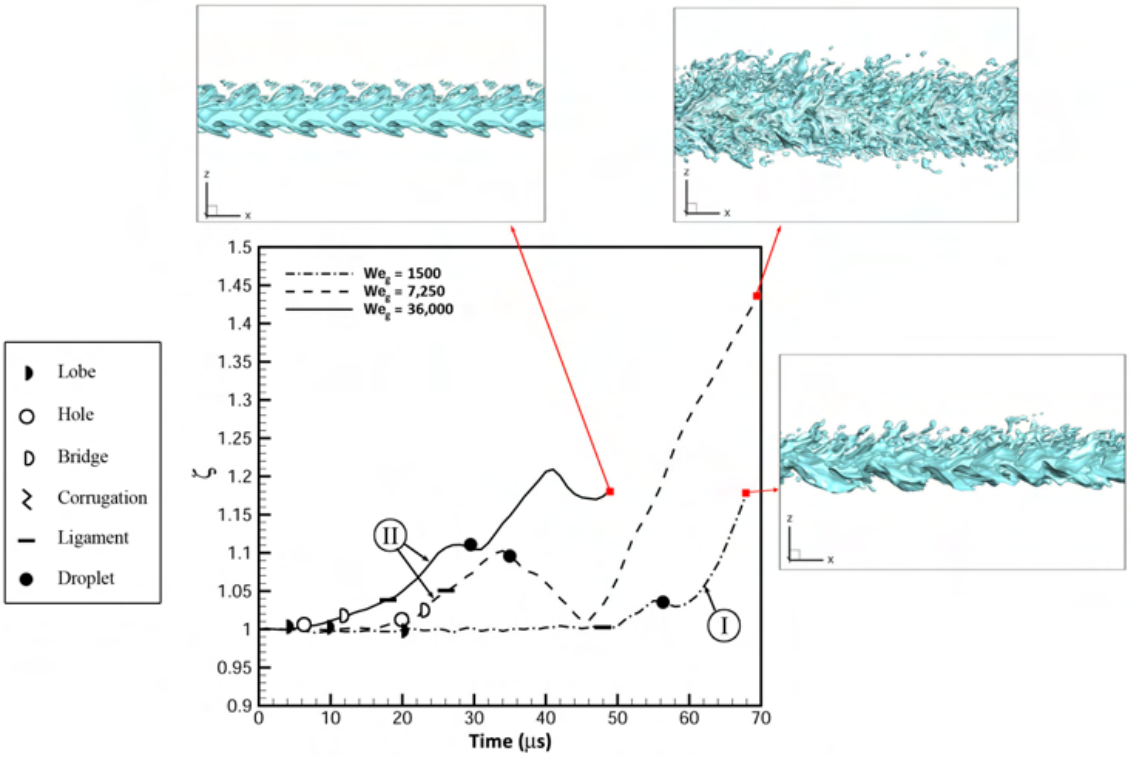

FIGURE 9. Average dimensionless spray size ζ variation with time for $We_g = 1500$, 7250, and 36 000; $Re_l = 2500$, $\hat{\rho} = 0.5$, $\hat{\mu} = 0.0066$, and $\Lambda = 2.0$. The liquid jet surface is shown at the end of each process. The symbols indicate the first time when different liquid structures form.

are also observed. With time, the peak of the initial distribution curve decreases while the distribution broadens. This decrease occurs faster at higher We_g, since the spray grows faster for lower surface tension. At $t = 50$ μs, only 8% of the liquid surface, i.e. computational cells at the interface, lie near the initial thickness for $We_g = 36\ 000$ (black solid line in figure 10*c*), and the spray has grown upto three times the initial sheet thickness; i.e. $h/h_0 \approx 3$. At the same time, the farthest normal distance reached by the liquid is about $2.8h_0$ from the centerplane for $We_g = 7250$; see where the dashed-line in figure 10(*b*) meets the horizontal axis. At still lower We_g, the maximum spray size is just slightly more than $2h_0$ at 50 μs, and still more than 16% of the liquid surface lies around the initial sheet thickness; see figure 10(*a*).

Figure 10(*b*) shows a missing section (having zero probability) around $1.4 < h/h_0 < 1.8$ at $t = 30$ μs. The same missing section moves to the right (to $1.5 < h/h_0 < 2.0$) at $t = 40$ μs, and finally vanishes at 50 μs. These sections - marked as the "first breakup" - coincide with the places where the sudden decrease in the average jet size was seen in figure 9 for $We_g = 7250$, explaining the oscillations in the average spray size. The missing section appears since some part of the liquid jet (ligament, bridge or droplet) detaches from the jet core and is entrained by the gas flow, leaving behind a vertical gap empty of any liquid surface at the breakup location, as shown in the sequential liquid surface images in figure 11.

The lobes form and stretch until about 25 μs, resulting in an increase in the average sheet thickness. At $t = 30$ μs (figure 11*b*), the bridge breaks from the lobe and creates a gap near the detachment location, where there are no liquid elements. Therefore, the average spray size suddenly drops at that time, even though the distance of the farthest liquid element from the centerplane is still increasing; i.e. the intersection of the PDF curves with the horizontal axis in figure 10(*b*) moves to the right. While the detached liquid blob moves away from the interface, the jet surface stretches outward again due

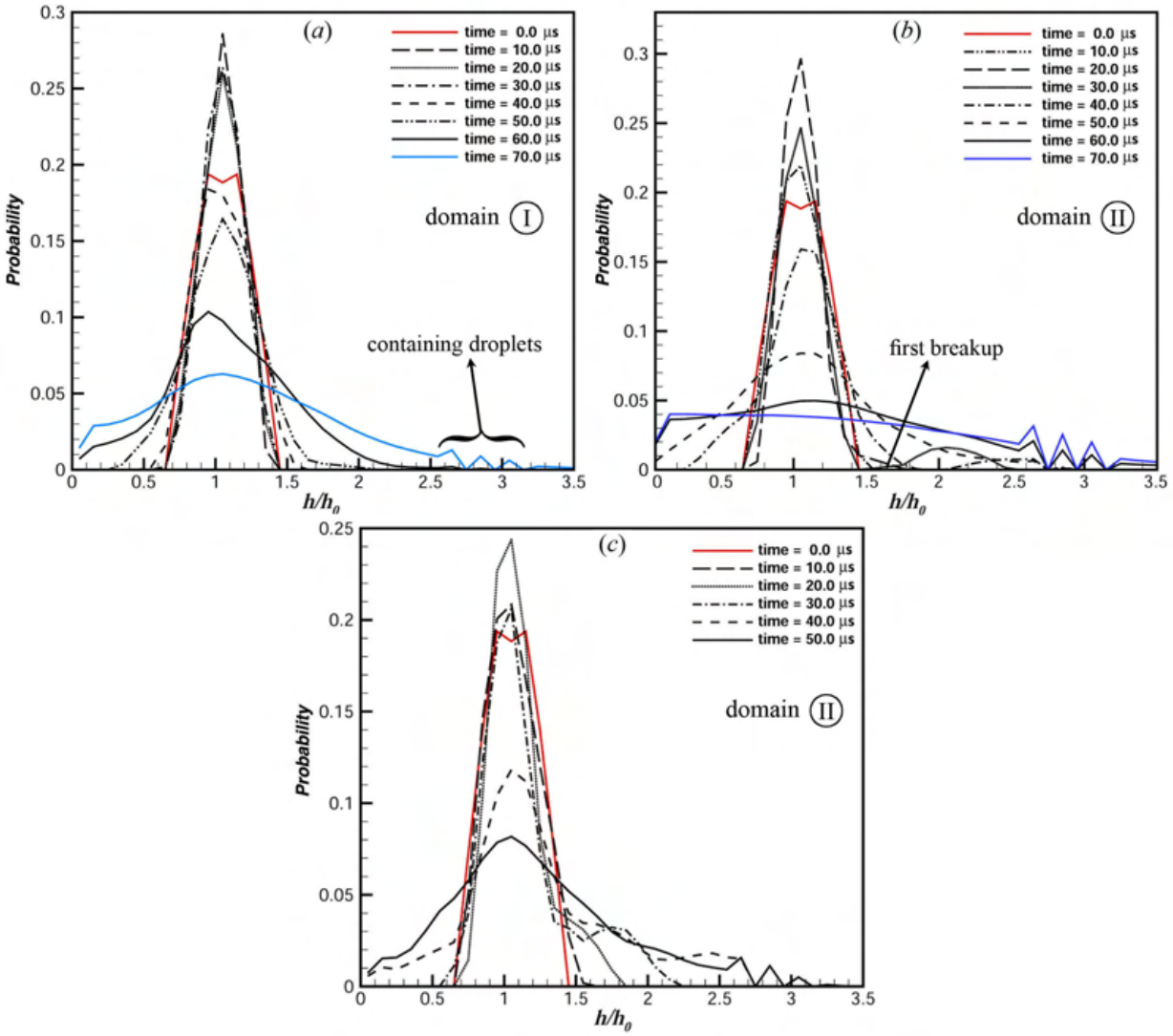

FIGURE 10. Nondimensional spray-size probability distribution at different times for $We_g = 1500$ (a), $We_g = 7250$ (b), and $We_g = 36\ 000$ (c); $Re_l = 2500$, $\hat{\rho} = 0.5$, $\hat{\mu} = 0.0066$, and $\Lambda = 2.0$.

to KH instability; the missing zone moves outward following it (figure 11c). The average spray size grows again when the new lobes and ligaments stretch enough to compensate for the broken (missing) section. At this time, the lobes and ligaments fill in the missing gap while the broken liquid structures advect farther from the interface, as shown in figure 11(d) at 50 μs.

The PDFs and the average spray-size plots indicate the first instance of ligament/bridge breakup, when the average spray size ζ starts to decline. Since the lower We_g case has less stretching and fewer ligament detachments at early time - due to the high surface tension - its spike is less intense and also appears much later (around 55 μs). The higher We_g, however, breaks much sooner at around 25 μs.

There are also some later oscillations near the maximum spray size of the probability distribution plots (see figure 10), for all three cases. The reason for these spikes is explained using the liquid iso-surface at 70 μs for $We_g = 1500$, illustrated in figure 12. The locations $2.5h_0$ and $3.0h_0$ are marked with the red lines. Undulations in the PDF curve occur in this range; see the blue line in figure 10(a) marked as "containing droplets". This range is mostly empty of liquids, i.e. filled with gas, except for very few cells which contain the occasional droplets or detached ligaments. In the spray PDF

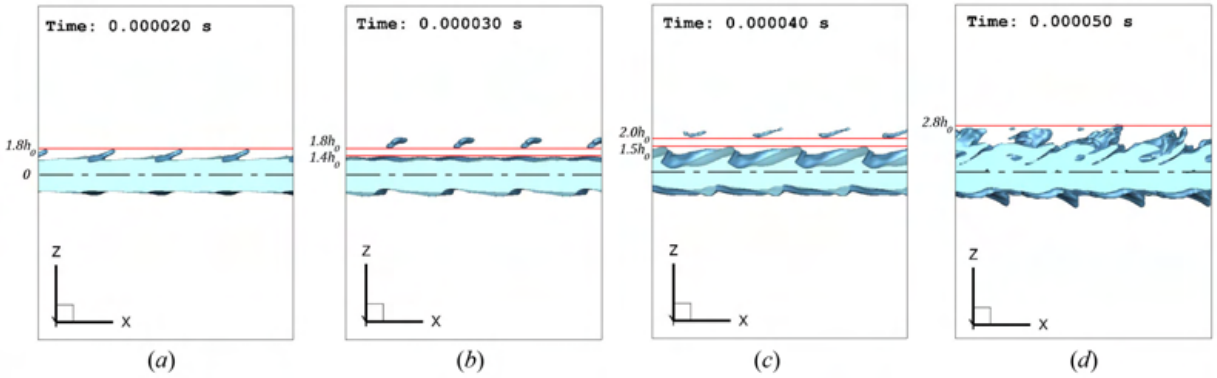

FIGURE 11. Side view of the liquid sheet surface at $t = 20$ µs (a), 30 µs (b), 40 µs (c), and 50 µs (d); $Re_l = 2500$, $We_g = 7250$, $\hat{\rho} = 0.5$, $\hat{\mu} = 0.0066$, and $\Lambda = 2.0$. Gas flows from left to right.

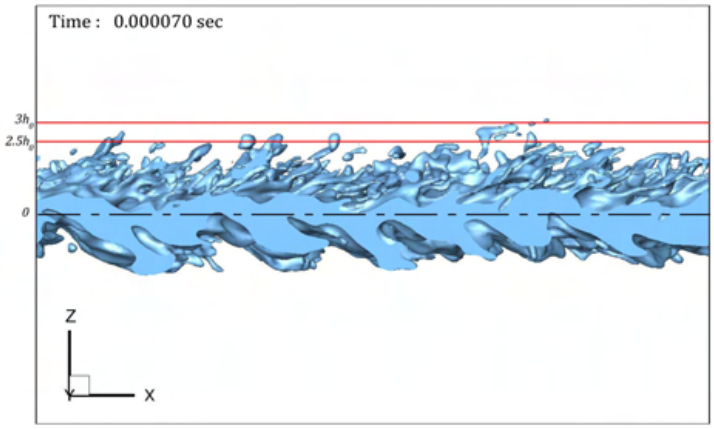

FIGURE 12. Side-view of the liquid surface at $t = 70$ µs; $We_g = 1500$, $Re_l = 2500$, $\hat{\rho} = 0.5$, $\hat{\mu} = 0.0066$, and $\Lambda = 2.0$. Gas flows from left to right.

plot, the empty spaces have zero or almost negligible probability, while other locations containing liquid droplets and broken ligaments have greater probability. Thus, waviness is seen in the spray size probability distribution at later times and at greater distances from the centerplane. Those spikes represent the droplets that are thrown outward, away from the liquid core centerplane, as the spray expands.

The reason for having non-zero probability for zero thickness in the PDF plots of figure 10 can also be assessed in figure 12. Since the antisymmetric mode is dominant in the considered range of Re_l and We_g, the trough of the surface wave reaches the centerplane (indicated by the broken line in figure 12) and even crosses it. Thus, after some time, non-zero probabilities occur for the surfaces that intersect the center-plane.

Figure 13 shows the standard deviation of the spray-size PDFs of figure 10. Initially, the standard deviation is below $0.2h_0 = 10$ µm, which is exactly equal to the amplitude of the initial perturbations. At early times, as the waves stretch in the streamwise direction, the amplitude of the waves decreases; hence, a larger portion of the interface gets closer to the initial sheet surface. This reduces the standard deviation of the spray size. This reduction is greater for lower We_g because of the stabilizing role of surface tension. Later, as the spray expands, the distance between the outer-most and the inner-most liquid surface grows, and the spray-size PDF gets wider; see figure 10. The deviation from the mean spray size increases with We_g.

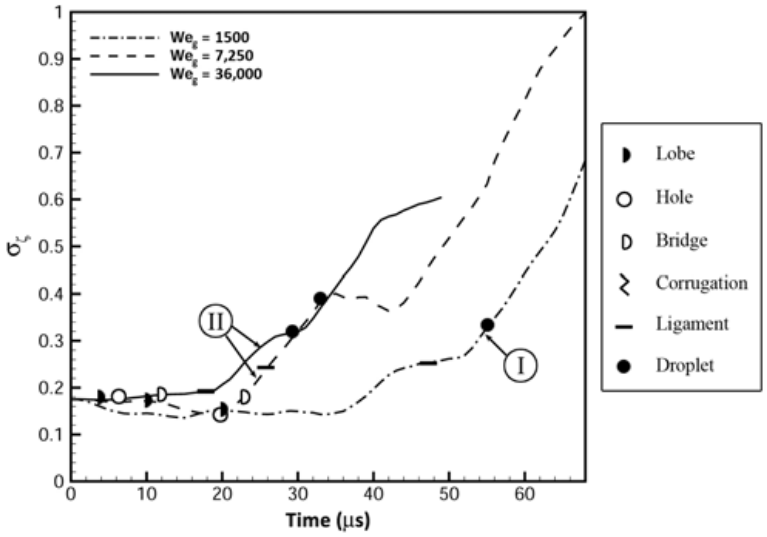

FIGURE 13. Temporal variation of the standard deviation of the dimensionless spray-size PDFs of figure 10 for $We_g = 1500$, 7250, and 36 000; $Re_l = 2500$, $\hat{\rho} = 0.5$, $\hat{\mu} = 0.0066$, and $\Lambda = 2.0$.

3.3. *Reynolds number effects*

Practically, Re_l should have a major effect on both the final droplet size and the spray angle as well as the rate of spray size growth or liquid structure cascade, since both the inertia and viscous effects are involved in these quantities. These effects are studied in this section with quantitative measures. Three different Re_l's are compared in this study; $Re_l = 1000$, 2500, and 5000 - each representing one of the domains in the We_g vs. Re_l plot with a particular breakup characteristic, as defined by Zandian *et al.* (2017*b*). $Re_l = 5000$ (in Domain III) and $Re_l = 1000$ (in Domain I) have the stretching characteristics during the primary breakup, with and without the corrugation formation, respectively. The $Re_l = 2500$ case follows the hole/bridge formation mechanism in Domain II.

Figure 14(*a*) demonstrates the effects of Re_l on the average length scale variation in time. As expected, the liquid surface is stretched more in the streamwise direction with increasing Re_l, creating flatter surfaces early on. Thus, as Re_l increases, relatively larger length scales occur at early times. For higher Re_l, the lobes stretch for a longer time before breakup, yielding maximum length scale at a later time. The actual breakup process and decrease of length scales occur later for higher Re_l; see figure 14(*a*).

After the early injection period, the rate of cascade of the large liquid structures, e.g. lobes and bridges, into smaller structures, e.g. corrugations, ligaments and droplets, is greater at higher Re_l, as observed from the mean slope in figure 14(*a*) in the downfall portion of the plot. By decreasing the liquid viscosity, i.e. increasing Re_l, with the other properties held constant, the breakup occurs faster and the rate of cascade of length scales grows. Figure 14(*a*) also shows that Re_l does not significantly affect the ultimate mean length scale after a long time. All three cases asymptotically reach a mean length scale of about $0.12\lambda_0$, although at different rates. However, the actual finest length scale in the distribution gets smaller and the largest length scale gets larger asymptotically, as Re_l increases.

Even though the formation of lobes is not affected much by Re_l, the ligaments and droplets form notably later as Re_l increases. This counter-intuitive fact is related to the process of ligament and droplet formation. At a constant We_g, the ligament formation in the *LoCLiD* process is slower than in the *LoHBrLiD* process, and both are slower than that in the *LoLiD* process. The mechanism of all these cascade processes are explained via vortex dynamics by Zandian *et al.* (2017*a*). The formation of corrugations at higher

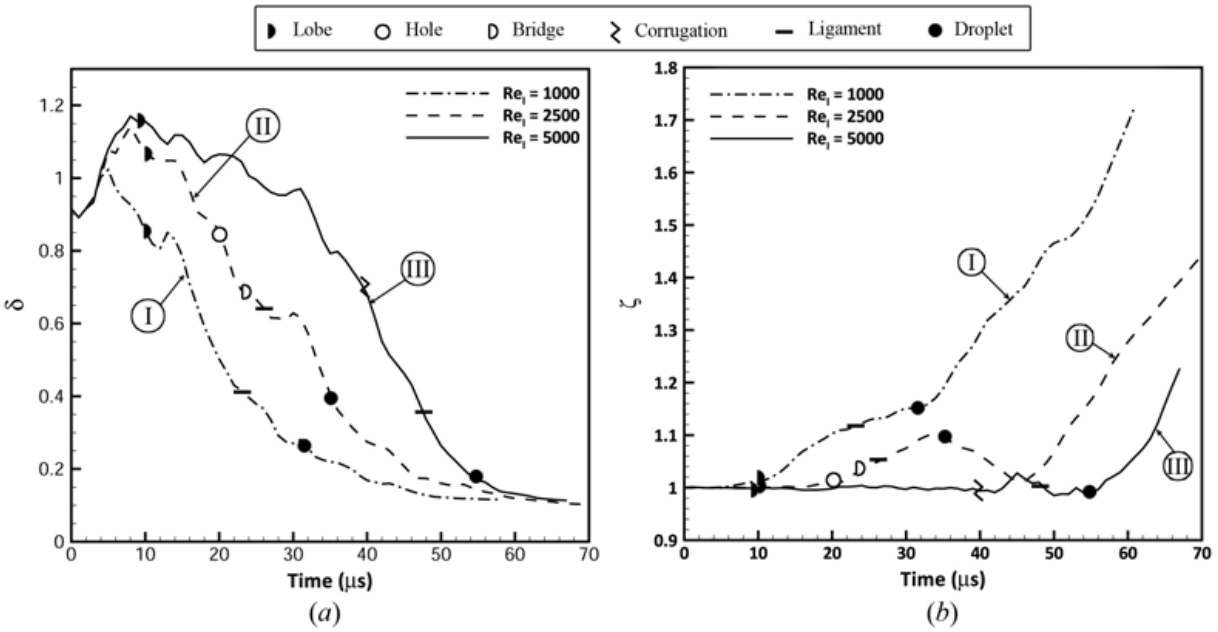

FIGURE 14. Effect of Re_l on the temporal variation of the average dimensionless length scale (a) and the average dimensionless spray size ζ (b); $We_g = 7250$, $\hat{\rho} = 0.5$, $\hat{\mu} = 0.0066$, and $\Lambda = 2.0$. The symbols indicate the first time when different liquid structures form.

Re_l takes longer and requires downstream advection of the split KH vortex by a distance of one wavelength (100 μm), until the hairpin vortices get undulated and induce the corrugations (Zandian *et al.* 2017*a*). The *LoHBrLiD* process, on the other hand, requires only stretching and overlapping of the hairpins over the KH vortices, which occur faster. The *LoLiD* mechanism involves cross-flow advection of the KH vortices, which occurs slightly more quickly. However, the droplets formed in the *LoCLiD* process are smaller than in the other two processes, and the *LoLiD* process results in the thickest ligaments and the largest droplets.

To better understand the difference in the mean length scale at the three Re_l's at early injection stage, the length scale PDFs for these cases are plotted at 5 μs and 10 μs in figure 15. Both times are within the initial injection period when the maximum length scale occurs; see figure 14(a). The $Re_l = 1000$, 2500, and 5000 cases are shown by red, black, and blue lines in figure 15, respectively. The PDFs are denoted by solid lines at 5 μs and dashed lines at 10 μs.

The highest Re_l (blue line) has the highest probability of larger length scales ($L/\lambda_0 > 2.0$) at both 5 μs and 10 μs, confirming the earlier claim that higher Re_l causes more stretched surfaces and larger scales (less curved surfaces) early on. Even though the maximum distribution of the length scales moves to smaller scales from 5 μs to 10 μs for $Re_l = 5000$, the average scale still grows, as shown in figure 14(a). In particular, a large population of the cells contains surfaces with very large length scales. As Re_l decreases, transition towards smaller scales occurs faster at these early times. Hence, the mean length scale decreases sooner for lower Re_l. Clearly, there are two factors in determining the mean length scale: the smallest and the largest length scales, and their populations. At an early stage, i.e. $t < 10$ μs, the smallest as well as the largest length scales are the same for all cases; however, it is the population of those small scales compared to the large ones that determines the mean scale. Since there are more large lengths at higher Re_l, more time is needed for those structures to cascade to smaller scales; thereby, the mean length scale keeps growing for a longer period at higher Re_l. After this initial period, however, the cascade is faster for the higher Re_l and the smallest bin gets populated at

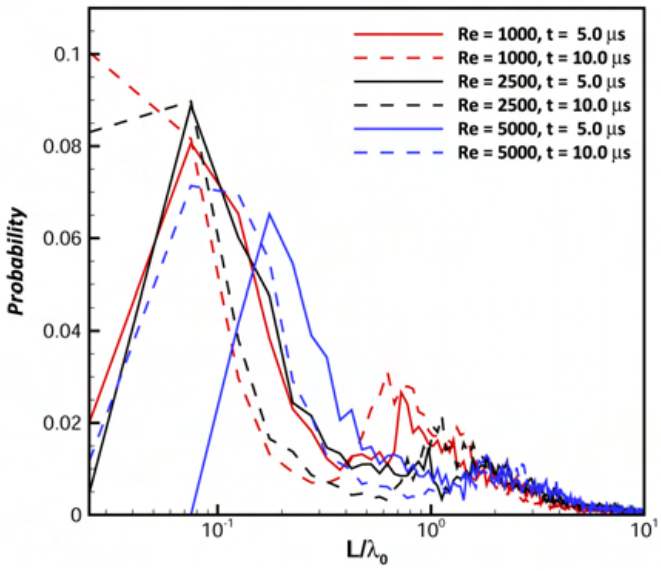

FIGURE 15. Probability distribution of the normalized length scales at $t = 5$ μs (solid lines) and 10 μs (dashed-lines) for $Re_l = 1000$ (red line), $Re_l = 2500$ (black line), and $Re_l = 5000$ (blue line); $We_g = 7250$, $\hat{\rho} = 0.5$, $\hat{\mu} = 0.0066$, and $\Lambda = 2.0$.

a higher rate. This means that the cascade of structures is faster at higher Re_l because there is less viscous resistance against surface deformation.

In the above results, there are two stages in the liquid-sheet distortion: (i) the initial stage of distortion when the lengths grow, and (ii) the final asymptote in time. Viscosity but not surface tension is dominant in the first stage, which is inertially driven, while surface tension more than viscosity affects the mean scale at the end.

Figure 14(b) shows the effects of the liquid viscosity on jet expansion. Since liquid inertia dominates the viscous effects at higher Re_l, the spray is oriented more in the streamwise direction, and the mean spray size and accordingly the spray angle are smaller at higher Re_l. This is consistent with both numerical simulations (Jarrahbashi *et al.* 2016) and experimental results (Carvalho *et al.* 2002; Mansour & Chigier 1990). Mansour & Chigier (1990) and Carvalho *et al.* (2002) showed that the spray angle is reduced by increasing the liquid velocity (or mass flow-rate); i.e. increasing Re_l. However, they only reported the final spray angle, but not its temporal growth. We show that the growth rate of the spray angle is lower at higher Re_l. The expansion of the spray starts much sooner in Domain I than in Domains II and III; however, the asymptotic spray growth rate is nearly the same for all three cases.

Even though both the lowest and the highest Re_l's produce similar lobe stretching mechanisms, there is a significant difference in their spray expansion. At high Re_l, the corrugations on the lobes stretch into streamwise ligaments, resulting in thinner and hence shorter ligaments. The time lapse between ligament formation and ligament breakup is much shorter in Domain III since the ligaments are generally shorter and need less time to thin and break. At low Re_l, on the other hand, the lobes directly stretch into ligaments, and the stretching is oriented in the normal direction as the viscous forces resist streamwise stretching caused by the inertia. It takes more time for the ligaments to break up into droplets. The ligaments are generally thicker and longer, as also shown for low Re_l by Marmottant & Villermaux (2004). This difference originates from the difference in the vortex structures of these two regimes, and shows that these two mechanisms have different causes from vortex dynamics perspective. For example, the streamwise vortex stretching is stronger at higher Re_l, causing streamwise oriented ligaments, as explained by Zandian *et al.* (2017a).

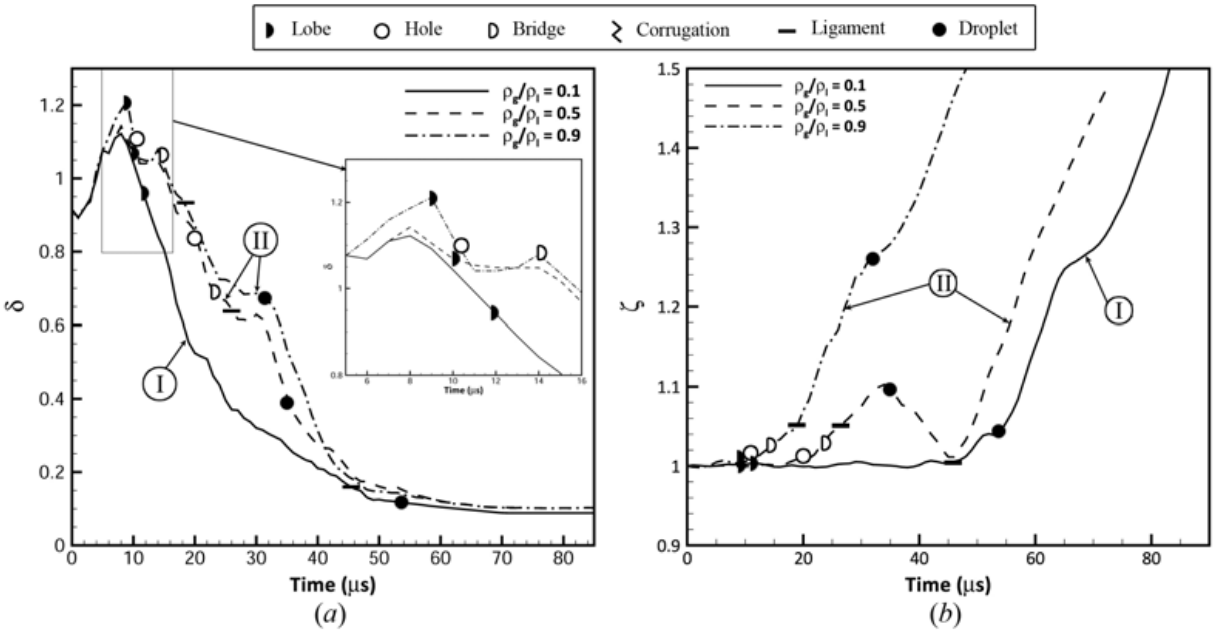

FIGURE 16. Effect of density ratio on the temporal variation of the average dimensionless length scale (a) and the average dimensionless spray size ζ (b); $Re_l = 2500$, $We_l = 14\ 500$, $\hat{\mu} = 0.0066$, and $\Lambda = 2.0$. The symbols indicate the first time when different liquid structures form.

3.4. *Density-ratio effects*

Effect of density ratio ($\hat{\rho}$) on the average liquid jet length scale is shown in figure 16(a). Three density ratios are studied here in a range of 0.1 (low gas density) to 0.9 (high gas density). The liquid Weber number, and thereby the surface tension coefficient are kept the same for all three cases; thus, We_g is also different for these three cases through gas density. The lowest $\hat{\rho}$ case falls in Domain I, where the lobes stretch directly into ligaments, and the other two high density ratios belong to Domain II, and involve hole and bridge formation in their breakup; see figure 2.

$\hat{\rho}$ has only a slight effect on the final length scale. All cases asymptotically reach a nearly similar average length scale of about $0.12\lambda_0$, with the final length scale being slightly smaller ($\approx 0.11\lambda_0$) for the lowest $\hat{\rho}$ (solid line in figure 16a). However, $\hat{\rho}$ clearly affects the rate at which the final length scale is achieved. The rate of length-scale reduction is higher at lower gas densities. As $\hat{\rho}$ increases, the cascade of length scales becomes slower. The asymptotic length scale is achieved at 50 μs for $\hat{\rho} = 0.1$, but at 56 μs for $\hat{\rho} = 0.5$, and at 60 μs for $\hat{\rho} = 0.9$. As denoted by the symbols in figure 16(a), the rate of ligament and droplet formation is notably affected by $\hat{\rho}$. As $\hat{\rho}$ grows, so that the Domain changes from I to II, the ligament and droplet formation rates undergo a large jump. As $\hat{\rho}$ keeps increasing in the same Domain (II), the ligaments and droplets form faster, but the difference is not as notable as the jump during the domain transition.

$\hat{\rho}$ does not alter the initial length scale growth significantly - the maximum scale occurs at nearly the same time - which proves it to be correlated with the liquid inertia and not the gas inertia. The asymptotic stage is also driven by the liquid inertia and is almost independent of the gas density in the $\hat{\rho}$ range considered here. As shown in §3.2, this stage is also correlated with surface tension. Therefore, the liquid Weber number (We_l) and not the gas Weber number (We_g) is the key parameter in determining the asymptotic droplet size; this will be elaborated in this section.

Figure 16(b) shows the temporal variation of the average spray size for low, medium, and high density ratios. The mean expansion rate increases with increasing $\hat{\rho}$, similar to the findings of Jarrahbashi *et al.* (2016) for round jets. The jet with the highest $\hat{\rho}$

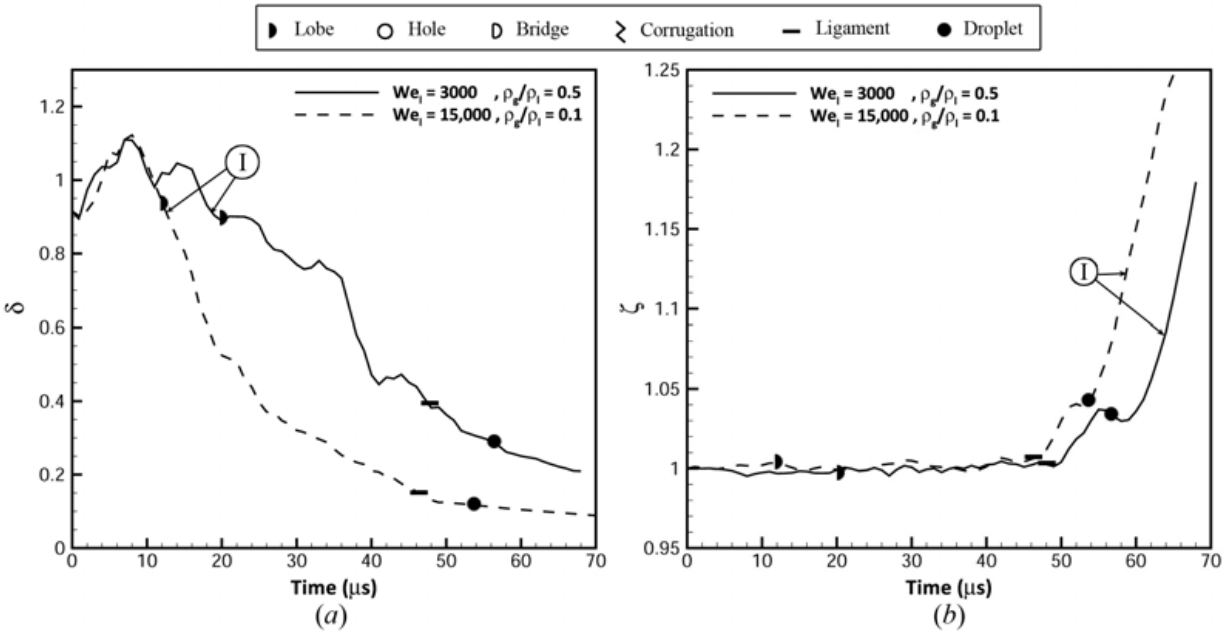

FIGURE 17. Effects of density ratio and We_l on the temporal variation of the average dimensionless length scale (a) and the average dimensionless spray size ζ (b); $Re_l = 2500$, $We_g = 1500$, $\hat{\mu} = 0.0066$, and $\Lambda = 2.0$. The symbols indicate the first time when different liquid structures form.

(dash-dotted line in figure 16b), which resembles homogeneous liquid jet, expands much more rapidly than the case with smaller $\hat{\rho}$ (solid line). The spray size grows from its initial thickness at 10 μs for the highest $\hat{\rho}$, while the expansion is postponed to 45 μs for the lowest $\hat{\rho}$. Some researchers have reported growth of the spray angle with increasing $\hat{\rho}$ or gas-to-liquid momentum ratio (Carvalho *et al.* 2002; Jarrahbashi *et al.* 2016) - based on the final stage of the expanded jet - but none has shown the temporal growth of the spray to be correlated with $\hat{\rho}$. Our results show that the jet expansion rate is also higher at higher $\hat{\rho}$.

Even though the average spray expansion rate is lower for lower gas densities, the asymptotic expansion rate is approximately the same after a long time from the start of the injection, regardless of $\hat{\rho}$. This is seen from the slopes of the curves in figure 16(b), which become approximately equal near the end of the computations; i.e. the asymptotic slopes appear to be independent of the gas density. Jarrahbashi *et al.* (2016) also found that the spray expansion rate is higher at higher $\hat{\rho}$ for circular jets. However, they used the traditional definition for the jet size, i.e. distance of the farthest continuous liquid structure from the centerline, which would be ambiguous in some cases, as discussed.

The lower expansion rate for low $\hat{\rho}$ is directly related to the vortex dynamics near the interface, studied in detail by Zandian *et al.* (2017a). The main cause of the lower expansion is the baroclinic effects which are drastically different amongst the range of density ratios considered here. Due to the larger density gradient, the baroclinic torque is higher at low gas densities. Thus, the vortex cores locate farther away from the interface (Zandian *et al.* 2017a). The induced flow of the vortices away from the interface entrains more gas into the mixing layer and expedites the two-phase mixing (Jarrahbashi *et al.* 2016; Zandian *et al.* 2017a). However, if the vortices remain closer to the interface, as in higher gas densities, KH roll-up occurs more vigorously, causing a faster cross-flow expansion of the jet (for detailed analysis of vortex dynamics and its connection with surface dynamics, see Zandian *et al.* 2017a).

Since an increase in $\hat{\rho}$ increases the spray size and expansion rate, and the sheet

expansion is also directly proportional to the liquid We (shown in §3.2), both We and $\hat{\rho}$ move in the same direction in relation with the jet expansion. It is interesting now to examine the effects of We and $\hat{\rho}$ combined through the gas-phase Weber number (We_g). This is demonstrated in figure 17(b), where the temporal evolution of the spray size for two cases that overlap at the same point in the We_g–Re_l map of figure 2 are compared. Both cases have the same $We_g = 1500$, but different $\hat{\rho}$ and We_l. Since $We_g = \hat{\rho} We_l$, density ratio and We_l should change in opposite directions to keep We_g constant; i.e. as $\hat{\rho}$ increases (increasing the jet expansion), We_l should decrease (decreasing the jet expansion). Figure 17(b) shows that the two cases behave very similarly in temporal expansion; both sprays expand at almost the same time and at the same asymptotic rate. The rate of ligament and droplet formation is also comparable in these two cases. This is consistent with the findings of Zandian *et al.* (2017a). Based on equation 3.1, the ligament stretching time scale τ_s is inversely proportional to Re_l, but independent of the Weber number. Since both cases in figure 17 have equal Re_l, their ligament stretching rates are also nearly equal. Therefore, the two parameters, We_l and $\hat{\rho}$, could be combined into a single parameter We_g for the matter of jet expansion analysis. The gas inertia (and not the liquid inertia) and liquid surface tension are the key parameters in determining the spray size. This confirms We_g to be the proper choice for categorizing the liquid-jet breakup characteristics, as used by Zandian *et al.* (2017b).

In §3.2, it was shown that a decrease in surface tension reduces the asymptotic droplet size and the average liquid-structures length scale. $\hat{\rho}$, however, has negligible effects on the average length scale. Thus, We_l is expected to be the key player in determining the final droplet size. Figure 17(a) confirms this notion and shows that even though the two cases have the same We_g, they manifest a significant difference in the cascade process and the final length scale. Since the case with a higher $\hat{\rho}$ has a lower We_l - keeping We_g constant - it produces larger average length scales and has a slower cascade. Thus, the liquid inertia is also important for the liquid structure cascade. Even though two jets at the same Re_l and We_g exhibit the same atomization mechanism (both from Domain I), the length scales of the resulting liquid structures depend on the density ratio. The lower gas density would result in finer structures. In other words, the atomization domain only determines the breakup quality (the type of process during the cascade), but other factors need to be considered to control the quantitative characteristics of the atomization; e.g. droplet size and structure length scales.

3.5. *Viscosity ratio effects*

Stapper *et al.* (1992) showed that viscosity ratio ($\hat{\mu}$) has little or no effect on the final droplet size (i.e. Sauter Mean Diameter, SMD) of liquid jets. Here, the same conclusion is reached, as shown in figure 18(a). A wide range of viscosity ratios $0.0005 < \hat{\mu} < 0.05$ covering three orders of magnitude are compared here. All cases follow the same cascade with an almost equal rate. The cascade is delayed less than a few microseconds in the period 10–40 μs for higher $\hat{\mu}$, but the small difference vanishes at later times. The asymptotic length scale is the same for all viscosity ratios, i.e. about $0.12\lambda_0 = 12$ μm, and the rate of droplet formation also remains the same regardless of $\hat{\mu}$. The gas viscosity is the least important factor in determining the droplet size and has no effect on the structure stretching and length scale growth in the initial stage; i.e. $t = 0$–10 μs.

Moreover, $\hat{\mu}$ does not have a notable influence on the expansion rate of the sheet either. As plotted in figure 18(b), the sheet expands at the same time regardless of the gas viscosity. The growth rate of the sprays, i.e. the slopes of the lines in figure 18(b), are also the same at the end of the process for all viscosity ratios. The only minor difference is that the spray growth gets delayed a few microseconds as gas viscosity increases. This minor

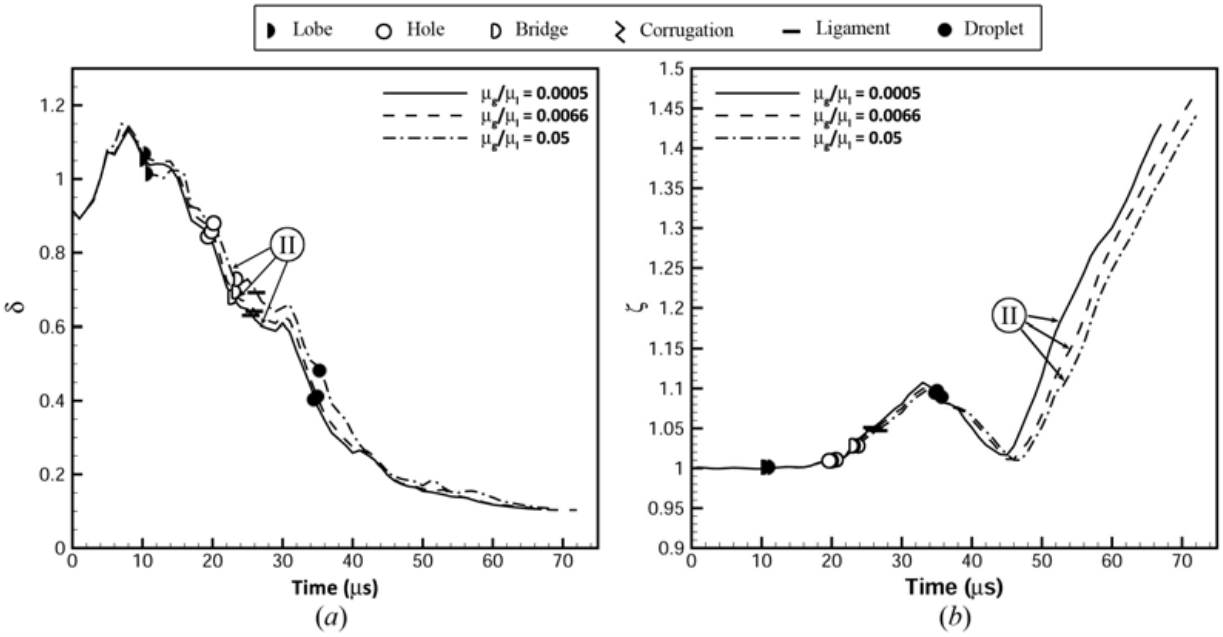

FIGURE 18. Effect of viscosity ratio ($\hat{\mu}$) on the temporal variation of the average dimensionless length scale (a) and the average dimensionless spray size ζ (b); $Re_l = 2500$, $We_g = 7250$, $\hat{\rho} = 0.5$, and $\Lambda = 2.0$. The symbols indicate the first time when different liquid structures form.

variation over three orders of magnitude $\hat{\mu}$ variation is insignificant and can be easily neglected. Therefore, the gas viscosity is not important in determining the spray angle and its growth rate, and the mean droplet size. The importance of viscosity only manifests through Re_l, where an increase in the liquid viscosity, i.e. lowering Re_l, increases the size of droplets and increases the spray angle and its growth rate, as discussed in §3.3.

3.6. *Sheet thickness effects*

Senecal *et al.* (1999) showed that ligament diameter is directly proportional to the initial sheet thickness. Our results, illustrated in figure 19(a), confirm their findings; the length scales grow as the sheet thickens. For this comparison, two sheets of different sizes have been analyzed - a thin sheet of 50 μm thickness with $\Lambda = 2.0$ and a thick sheet of 200 μm thickness with $\Lambda = 0.5$. The initial perturbation wavelength is the same for both cases; i.e. $\lambda_0 = 100$ μm.

The cascade occurs much slower and the mean length scale oscillates more in its cascade process for the thicker sheet compared to the thin sheet; see figure 19(a). The extra oscillations found for the thicker sheets are because the initial KH waves take more time to stretch and break into smaller structures as sheet thickness increases. This is explained via vortex dynamics of the interface deformation, where the two vortex layers on top and bottom of the sheet become farther apart and more independent as the sheet becomes thicker. The interaction between the two vortex layers is more intense for the thinner sheets, and consequently the cascade occurs faster under the local induction of these two vortex layers (Zandian *et al.* 2017a). As the initial sinusoidal KH wave stretches in the streamwise direction, the curvature of the interface decreases and the mean length scale grows; as the waves curl over the vortices and the lobes form, the mean length scale decreases. If the waves dampen again, the length scale temporarily increases with it, until the next waves start to grow. The process of wave stretching and curling occurs continuously until the lobes stretch enough to cascade into smaller structures; e.g. ligaments and droplets. The length scale keeps on decreasing until the asymptotic length scale is achieved. Increasing sheet thickness also significantly delays

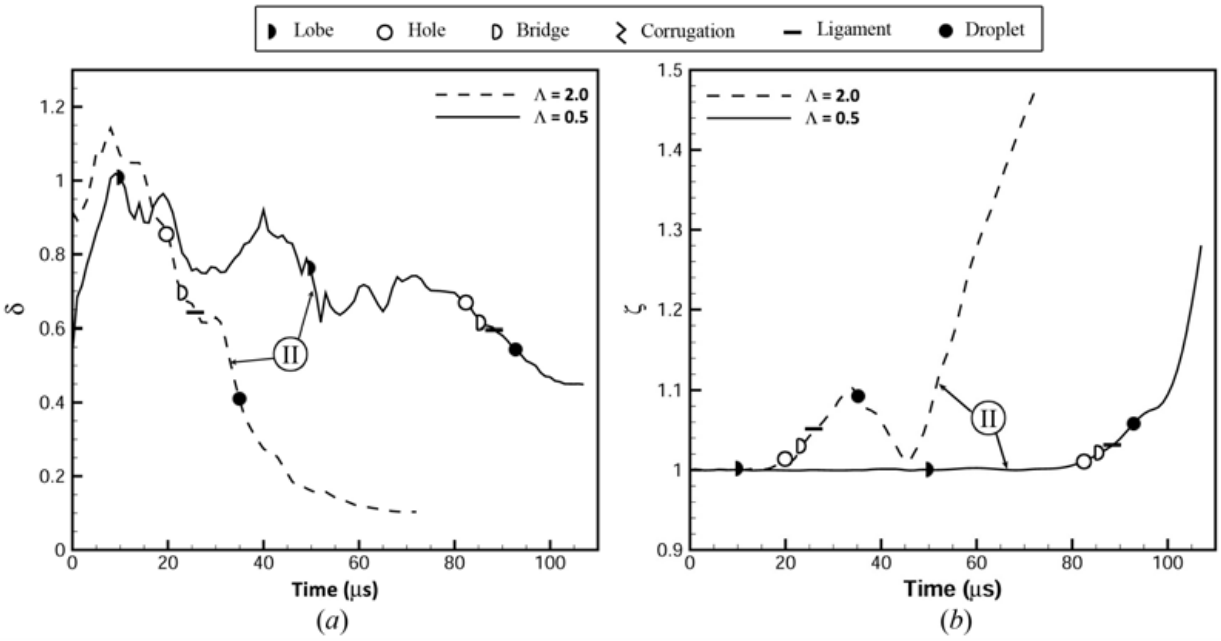

FIGURE 19. Effect of sheet thickness on the temporal variation of the average dimensionless length scale (a) and the average dimensionless spray size ζ (b); $Re_l = 2500$, $We_g = 7250$, $\hat{\rho} = 0.5$, and $\hat{\mu} = 0.0066$. The symbols indicate the first time when different liquid structures form.

the structure formations on the sheet surface. The lobes and ligaments form respectively 40 μs and 50 μs later on the thick sheet than on the thin sheet.

The asymptotic length scales for the thin and thick sheets are $0.12\lambda_0$ and $0.47\lambda_0$, respectively - agreeing with the findings of Senecal *et al.* (1999). Based on their analytical study, the ligament size should be directly proportional to the initial sheet thickness; thus, as the sheet becomes four times thicker, the mean ligaments size is predicted to increase by a factor of four. Since the larger length scales caused by the curvature of the waves are also included in our mean length scale calculation, the ratio of the mean length scale for the thick and thin sheets in our case is about 3.92 - in very good agreement.

The spray expansion is significantly delayed as the sheet thickness increases; see figure 19(b). While the thin sheet expands at 20 μs, the expansion of the thicker jet does not start until 80 μs. Even though a thin sheet has higher growth rate at the early stages of spray formation, the thicker sheet achieves the higher growth rate at the final stage. This is seen from the slopes of the solid and dashed-lines in figure 19(b) at the end of the processes, where the slope is higher for the solid line; i.e. the thick sheet. This major difference is caused by the reduced influence of the vortex layers in the thicker sheet, resulting in a slower shift towards antisymmetry as the vortex layers get farther apart. The mean spray size being normalized by the initial sheet thickness, the absolute growth rate of the thicker sheet in the final phase is much higher than the thin sheet. This situation develops after the vortices have grown sufficiently and the sheet has become totally antisymmetric. The wavelength of the most dominant antisymmetric instability waves are larger for thicker sheets (Zandian *et al.* 2016). Thereby, the growth rate of those larger waves are clearly higher than the short waves occurring in thin planar jets.

3.7. *SMD calculation*

For liquid jet atomization, the injector designer is usually interested in the average size based on mass distribution. Sauter mean diameter (SMD, d_{32}) is an average of particle size, defined as the diameter of a sphere that has the same volume/surface-area ratio as a particle of interest, and is a proper parameter for this purpose. The SMD is calculated

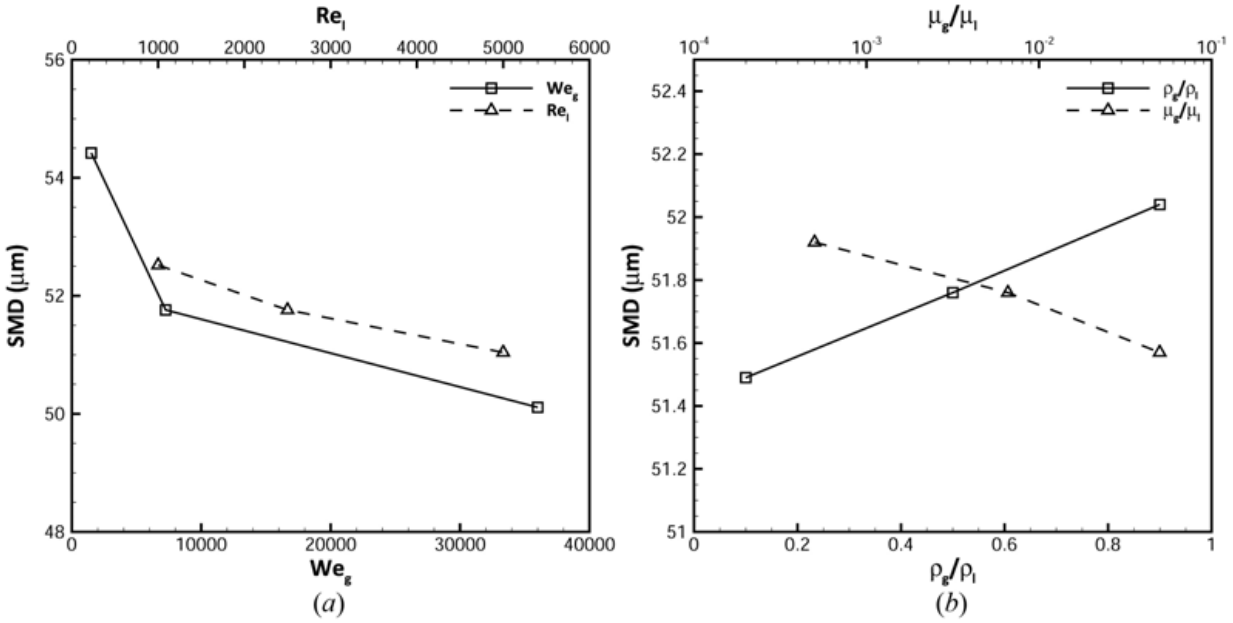

FIGURE 20. Effects of We_g and Re_l (a), and $\hat{\rho}$ and $\hat{\mu}$ (b) on SMD; $Re_l = 2500$, $We_g = 7250$, $\hat{\rho} = 0.5$, and $\hat{\mu} = 0.0066$.

using the following equation;

$$\text{SMD} = \frac{\Sigma_i N_i d_i^3}{\Sigma_i N_i d_i^2}, \tag{3.2}$$

where N_i is the number of droplets per unit volume in size class i, and d_i is the droplet diameter.

Similar to this definition, we calculate a SMD based on our length scale L_i and its probability $P(L_i)$;

$$\text{SMD} = 2\frac{\Sigma_i P(L_i) L_i^3}{\Sigma_i P(L_i) L_i^2}; \tag{3.3}$$

however, since L_i asymptotes to the droplet radius after all of the jet has broken into droplets, a coefficient of 2 is considered in equation (3.3) in order to obtain a mean diameter rather than radius. All the length scales greater than 100 μm are neglected in this analysis since those length scales are much larger than even the largest droplet diameters in our computations and do not represent droplets, but rather some other unbroken liquid structure. Consequently, the SMDs are expected to be larger than what they should be in such a parameter range, but these measures are reported as a tool for comparison. The SMDs are calculated after the asymptotic length scales are achieved.

The effects of We_g and Re_l on SMD are shown in figure 20(a). As expected, We_g has the more significant influence on SMD. SMD decreases from 54.5 μm to almost 50 μm as We_g is increased from 1500 to 36 000. Even though this decrease is not as huge as was predicted by Varga *et al.* (2003), its influence is more significant than of the other parameters. The dependence of SMD on We_g as given by Varga *et al.* (2003) is limited to a much smaller We_g range than considered in our study. At the higher range of We_g in our study, the effect of We_g is not as pronounced, though certainly not negligible.

Increasing Re_l also reduces SMD, as shown in figure 20(a). The difference in SMD is about a micron over the range of Re_l considered in this study; i.e. $1000 < Re_l < 5000$. However, Re_l clearly influences SMD and the final droplet size, as was discussed in §3.3, but not so obvious in figure 14(a). Both the range of SMD and its behavior with respect to Re_l are in agreement with Lozano *et al.* (2001).

Figure 20(b) shows the effects of density and viscosity ratios on the SMD. Both of these parameters have very minor influence on SMD compared to Re_l and We_g; even though $\hat{\mu}$ changes over three orders of magnitude and $\hat{\rho}$ ranges from 0.1 to 0.9, the difference in SMD is less than 0.5 μm. SMD slightly increases with increasing $\hat{\rho}$ and with decreasing $\hat{\mu}$, but the changes are insignificant. In the range that has been covered here, the dependence on $\hat{\rho}$ is almost linear, while the dependence on $\hat{\mu}$ is linear only on the log-basis.

4. Conclusions

Two PDFs were formed for the liquid-structure size and the spray size from the numerical data that was obtained from a time-variant three-dimensional direct numerical simulation on a liquid-sheet segment. The PDFs of the structure size provided statistical information about the droplet-size distribution and the qualitative number density of droplets in a liquid-jet atomization. The temporal variation of the mean of the PDFs gave useful information about the rate of cascade of liquid structures in different atomization domains. The mean and PDF of the spray size also showed the first instance of breakup of lobes and ligaments.

Our analysis accurately predicts the effects of gas Weber number (We_g), liquid Reynolds number (Re_l), density ratio, viscosity ratio, and the sheet thickness on the droplet size and the spray expansion. The results show that the final droplet size decreases with increasing We_g, and the cascade of structures happens faster for higher We_g. The spray size (spray angle) also grows at a higher rate for higher We_g. The initial growth of the length scales due to the stretching of the waves and lobes is affected by liquid inertia more than by the surface tension, while the asymptotic stage of length scale cascade is affected mostly by surface tension and liquid inertia, but less by liquid viscosity.

The liquid structure cascade rate is significantly increased by increasing Re_l. The spray size is larger at lower Re_l, and the spray angle and the rate of spray growth decreases as Re_l increases. Gas-to-liquid density ratio has minor influence on the final droplet size, but the cascade of length scales occurs slower as density ratio increases. Gas inertia and liquid surface tension are the key parameters impacting the spray size. The spray size grows significantly with increasing gas density. Viscosity ratio has negligible effect on both the spray size and the final droplet size. Increasing the sheet thickness, however, decreases both the spray size and its growth rate, while decreasing the structure cascade rate and producing larger droplets.

The cascade process and the spray expansion rate are decoupled for different atomization domains. Differences were notable for the length-scale distribution and spray expansion in different domains. The time of the length scale cascade and the sheet expansion was related to the formation of various structures in different domains.

REFERENCES

Carvalho, I. S., Heitor, M. V. & Santos, D. 2002 Liquid film disintegration regimes and proposed correlations. *International journal of multiphase flow* **28** (5), 773–789.

Desjardins, O. & Pitsch, H. 2010 Detailed numerical investigation of turbulent atomization of liquid jets. *Atomization and Sprays* **20** (4), 311–336.

Dombrowski, N. & Hooper, P. C. 1962 The effect of ambient density on drop formation in sprays. *Chemical Engineering Science* **17** (4), 291–305.

Hirt, C. W. & Nichols, B. D. 1981 Volume of fluid (vof) method for the dynamics of free boundaries. *Journal of computational physics* **39** (1), 201–225.

Jarrahbashi, D. & Sirignano, W. A. 2014 Vorticity dynamics for transient high-pressure liquid injection a. *Physics of Fluids* **26** (10), 73.

Jarrahbashi, D., Sirignano, W. A., Popov, P. P. & Hussain, F. 2016 Early spray development at high gas density: hole, ligament and bridge formations. *Journal of Fluid Mechanics* **792**, 186–231.

Lefebvre, A. H. 1989 Atomization and sprays. *New York: Hemisphere Publishing Corp.* **1989**.

Lozano, A., Barreras, F., Hauke, G. & Dopazo, C. 2001 Longitudinal instabilities in an air-blasted liquid sheet. *Journal of Fluid Mechanics* **437**, 143–173.

Mansour, A. & Chigier, N. 1990 Disintegration of liquid sheets. *Physics of Fluids A: Fluid Dynamics* **2** (5), 706–719.

Marmottant, P. & Villermaux, E. 2004 On spray formation. *Journal of fluid mechanics* **498**, 73–111.

Negeed, El-Sayed R., Hidaka, S., Kohno, M. & Takata, Y. 2011 Experimental and analytical investigation of liquid sheet breakup characteristics. *International Journal of Heat and Fluid Flow* **32** (1), 95–106.

Osher, S. & Fedkiw, R. P. 2001 Level set methods: an overview and some recent results. *Journal of Computational Physics* **169** (2), 463–502.

Rider, W. J. & Kothe, D. B. 1998 Reconstructing volume tracking. *Journal of computational physics* **141** (2), 112–152.

Scardovelli, R. & Zaleski, S. 1999 Direct numerical simulation of free-surface and interfacial flow. *Annual review of fluid mechanics* **31** (1), 567–603.

Senecal, P. K., Schmidt, D. P., Nouar, I., Rutland, C. J., Reitz, R. D. & Corradini, M. L. 1999 Modeling high-speed viscous liquid sheet atomization. *International Journal of Multiphase Flow* **25** (6), 1073–1097.

Stapper, B. E., Sowa, W. A. & Samuelsen, G. S. 1992 An experimental study of the effects of liquid properties on the breakup of a two-dimensional liquid sheet. *J. Eng. Gas Turbines Power* **114** (1), 39–45.

Sussman, M., Fatemi, E., Smereka, P. & Osher, S. 1998 An improved level set method for incompressible two-phase flows. *Computers & Fluids* **27** (5), 663–680.

Varga, C. M., Lasheras, J. C. & Hopfinger, E. J. 2003 Initial breakup of a small-diameter liquid jet by a high-speed gas stream. *Journal of Fluid Mechanics* **497**, 405–434.

Zandian, A., Sirignano, W. A. & Hussain, F. 2016 Three-dimensional liquid sheet breakup: vorticity dynamics. *AIAA Paper 2016-1593* .

Zandian, A., Sirignano, W. A. & Hussain, F. 2017*a* Explanation of liquid sheet breakup mechanisms via vortex dynamics. Journal of Fluid Mechanics.

Zandian, A., Sirignano, W. A. & Hussain, F. 2017*b* Planar liquid jet: early deformation and atomization cascades. Physics of Fluids (invited for revision).

Zhao, H. K., Chan, T., Merriman, B. & Osher, S. 1996 A variational level set approach to multiphase motion. *Journal of computational physics* **127** (1), 179–195.